UNIVERSIDAD
DE LA REPUBLICA
URUGUAY

Simulation of Vorticity Wind Turbines

A Coupled Discret Element Method and Finite Volume Method for the Simulation of Elastic Bodies

Paolo Juan Sebastián Sassi Arobba

Postgraduate Program in Energy Engineering
School of Engineering
University of the Republic

Montevideo – Uruguay
July 2017

UNIVERSIDAD DE LA REPUBLICA
URUGUAY

FACULTAD DE INGENIERIA

imfia

M F C

Simulation of Vorticity Wind Turbines

A Coupled Discret Element Method and Finite Volume Method for the Simulation of Elastic Bodies

Paolo Juan Sebastián Sassi Arobba

Master's Thesis presented to the Postgraduate program in Energy Engineering, from the School of Engineering at the University of the Republic, Uruguay, as a requisite for acquiring a Master degree in Energy Engineering

Director:
D.Sc. Prof. Jorge Freiría

Co-advisor:
D.Sc. Prof. Gabriel Usera

Academic director:
D.Sc. Prof. Gabriel Usera

Montevideo – Uruguay
July 2017

Sassi Arobba, Paolo Juan Sebastián

Simulation of Vorticity Wind Turbines / Paolo Juan Sebastián Sassi Arobba. - Montevideo: Universidad de la República, Facultad de Ingeniería, 2017.

XXIX, 87 p.: il.; 29, 7cm.

Director:

Jorge Freiría

Codirector:

Gabriel Usera

Director académico:

Gabriel Usera

Tesis de Maestría – Universidad de la República, Programa en Ingeniería de la Energía, 2017.

Referencias bibliográficas: p. 71 – 75.

1. Mecánica de los Fluidos Computacional, 2. Método de Elementos Discretos, 3. Método de Volúmenes Finitos, 4. Turbina Eólica de Vorticidad, 5. Red de Pesca. I. Freiría, Jorge, *et al.* II. Universidad de la República, Programa de Posgrado en Ingeniería de la Energía III. Título.

EXAMINING COMMITTEE

MSc. Prof. Mariana Mendina

Ph.D. Prof. Ildefonso Cuesta

Ph.D Prof. Pedro Galione

Montevideo – Uruguay
July 2017

To Luca and Gaspar.

Aknowledgment

First of all, I would like to thank Prof. Freiría and Prof. Usera, not only for accepting to foster and guide my research, but also for encouraging me to accomplish my Master degree, and for including me as a member of the group of computational fluid mechanics of the University. I also extend my gratitude to the Postgraduate Academic Commission (CAP) for all the confidence that they placed in me when they granted me a scholarship. I appreciate the continuous and relentless support that my family and loved ones have given me along the way, which helped me to stay focused on achieving my goal.

Throughout this research process, I had the great fortune of having very good professors who provided me the necessary tools to tackle the issues addressed in this thesis. I am deeply indebted to Prof. Mendina and Dr. Draper for being always eager to answer my questions about computing and modeling; to Prof. Solari for his very useful insights on structural topics; and to Prof. Cataldo for introducing me to the field of wind energy. I am also very grateful to the professors form the Mechanical Engineering and Industrial Production Institute (IIMPI) and the Electric Engineering Institute (IIE) for all their interesting lectures, that helped me through the years to expand my horizons as an Energy Engineer specialist.

I met numerous fellow students with whom I had the privilege of sharing hours of study and research, and who shaped my understanding of the matter to no lesser extent than the bibliography or the formal academic training. And, last but not least, I would like to acknowledge the fertile environment of the Department of Fluid Mechanics and Environmental Engineering of my University, in which the constructive atmosphere of cooperation imbues professors, staff and students in the same enthusiastic way.

"To those who do not know mathematics it is difficult to get across a real feeling as to the beauty, the deepest beauty, of nature ... If you want to learn about nature, to appreciate nature, it is necessary to understand the language that she speaks in."

Richard Feynman

"You never change things by fighting the existing reality. To change something, build a new model that makes the existing model obsolete."

R. Buckminster Fuller

ABSTRACT

Several devices and man-made structures interact dynamically with fluids such as water and air, behaving essentially as flexible elastic systems that undergo large deformations and complex dynamics. The design and analysis of the variable degrees of efficiency that these devices may have under different flow conditions can be carried out using numerical modeling tools. Devising ways of simulating the behavior of fluids with ever increasing accuracy is essential to save time and resources while testing the potential of new technologies. One of the fields of engineering that has shown most significant growth in recent years is the generation of energy from renewable sources. The present research adapts mathematical methods, still new to the field, to represent ways of dealing with flows of fluid in bidirectional interactions with those new technologies, and particularly applies them to the exploration of a new kind of vertical blade-less turbine that gathers energy from the vortex induced vibrations (VIV) of a relatively short and scalable mast. This device is very promising for several logistic and cost related reasons, especially when considering the difficulties of implementing new approaches in developing countries, but until now it has not been tested under rigorous theoretical models or with simulation methods that can have true predictive value. This research a) presents a framework for such modeling by coupling the discrete element method (DEM) with the finite volume method (FVM), b) compares the theoretical method with previous tests that had both computational and physical experiments to be contrasted, and c) suggests ways to make the technology more efficient and adaptable to changing conditions.

Keywords:
Computational Fluid Dynamics, Discrete Element Method, Finite Volume Method, Vorticity Wind Turbines, Fish Nets.

RESUMEN

Diversas estructuras y dispositivos creados por el hombre deben interactuar mecánicamente con fluidos, en particular agua y aire. Cuando estas estructuras constituyen además sistemas elásticos y flexibles, la interacción con fluidos involucra una dinámica doblemente compleja, pues los flujos generan deformaciones en las estructuras, que a su vez determinan y modulan las respuestas del fluido. Durante los procesos de diseño, el análisis de los respectivos grados de eficiencia que estos dispositivos alcanzarán bajo la acción de diversas condiciones de flujo, puede llevarse a cabo mediante herramientas de modelación numérica. Idear formas de simular la interacción de fluidos y estructuras con precisión resulta esencial para evitar inútiles pérdidas de tiempo y recursos a la hora de evaluar el potencial de nuevas tecnologías. Una de las ramas de la ingeniería que ha crecido de un modo más significativo en las últimas décadas es la generación de energía a partir de fuentes renovables. La presente investigación adapta métodos matemáticos de representación, todavía nuevos en el área, para simular la interacción fluido-estructura en esas nuevas tecnologías, y en particular los aplica a un nuevo tipo de turbina eólica sin aspas, que extrae energía a través de la vibracion inducida por el desprendimiento de vórtices (VIV) de un mástil vertical flexible. Esta tecnología se presenta como muy prometedora, tanto por razones de logística como de costo, especialmente si se consideran las dificultades para implementar nuevos recursos técnicos en países en desarrollo, pero hasta ahora no han sido evaluadas bajo modelos teóricos rigurosos o con métodos de simulación con verdadero valor predictivo. Esta tesis a) presenta un marco de referencia para este tipo de simulaciones acoplando el Método de Elementos Discretos (DEM) con el Método de Volúmenes Finitos (FVM), b) compara modelos teóricos de pruebas anteriores que contiene tanto experimentación física como computacional, lo que permite contrastar resultados, y c) sugiere formas de hacer esta tecnología mas eficiente y adaptable a condiciones variables.

Palabras claves:
Mecánica de los Fluidos Computacional, Método de Elementos Discretos, Método de Volúmenes Finitos, Turbina Eólica de Vorticidad, Red de Pesca.

List of Figures

List of Tables

List of symbols

List of the most relevant notations of the thesis

ξ_s Structural damping 29
D_M Diameter of the Mast 25
D_{ref} Reference diameter, $D_M(z_e)$ 25
D_r Diameter of the Rod 25
z_e Equivalent heigth of the structure 25, 52
F_{imb} Immersed boundary force 32, 37, 67
F_{em} Electro-magnetic force 38
f_N Natural frequency of the structure 25, 27
f Oscillatory frequency of the structure 52, 66
f_{vs} Frequency of the vortex shedding 27, 54, 66
L_M Length of the mast 24, 25
L_r Length of the rod 25
$m_{e,1}$ Equivalent mass per unit heigth 10, 27
m_1 Generalized mass 26
m Mass per unit heigth 27
M_{imb} Immersed boundary moment 37
P Instantaneous Power 39
η Instantaneous Efficiency 40
$\overline{P}$ Integrated Power 40
$\overline{\eta}$ Integrated Efficiency 40
Re Reynolds number 27, 28, 29, 30, 52, 66, 85
Sc Scruton number 10, 27, 29
St Strouhal number 28, 66
v_{cr} Critical velocity 28, 29

Acronyms

Lista of the mos relevant acronyms of this thesis

CFD Computational Fluid Dynamics 3, 66

DEM Discrete Element Method 4, 6, 15, 19, 20, 23, 30, 32, 35, 40, 41, 66

FVM Finite Volume Method 4, 6, 15

GHG greenhouse gas 3

IBM Immersed Boundary Method 4, 5, 17, 18, 31, 32, 37, 47, 51

LES Large Eddy Simulation 16, 51

MPI Message Passing Interface 16, 30

VIV Vortex-Induced Vibrations 2, 3, 4, 5, 7, 9, 12, 13, 23

VIVACE Vortex-Induced Vibrations Aquatic Clean Energy 12, 67

VWT Vorticity Wind Turbine 5, 6, 9, 10, 11, 18, 20, 23, 24, 30, 31, 40, 45, 52, 57, 59, 62, 66, 85, 87

Contents

Chapter 1

Introduction

1.1 Motivation

In recent decades, renewable energies had a great deal of expansion worldwide. The causes for this growth are varied and can be associated with several changes, such as:

- A rise in environmental awareness and related policies, as there is currently a strong global pressure to slow down global warming with international commitments to reduce emissions by setting targets and maximum agreed levels.
- An expected depletion of the natural resources currently used for power generation, such as coal and gas.
- The widespread adoption of new generation technologies that are gaining ground in the global market and consolidating their position in the mainstream. That includes not only a growing variety of devices and sources of generation but also the construction of dedicated infrastructure with growing sustainability as a matter of national policy.
- The technological advancement of classic renewable generation (traditional wind-turbines and solar panels) that have gained performance efficiency and thus improve their economic equation.
- A growing tendency to diversify the energy matrix in order to avoid dependence on highly fluctuating fossil markets.
- An ever-growing increment in energy demand, related to the development of emergent economies.
- A need for isolated generation in rural areas, away from transmission

lines, and even for micro-generation in urban areas, bypassing the construction or overloading of transmission and distribution networks.

During the current decade, Uruguay substantially changed its energy matrix at such dramatic pace that moved the country to the forefront of the global ranking of adoption of new sources and technologies, second only to some Scandinavian countries. A large investment in wind energy infrastructure, which added to the hydroelectric and thermal biomass generation already available, has shifted the matrix of renewable sources to an outstanding 95 percent of the national consumption of electricity, prompting the country to export energy to its neighbors for the very first time in history. Several factors have contributed to this process, but among those it is worth highlighting the body of research dedicated to such renewable sources and technologies.

Although there have been many substantial technical developments on large-scale wind generation, there are still no technologies with the same positive impact on the economic equation at the micro-generation level, either because of the long pay-back periods that small wind turbines involve or due to the susceptibility of these to the turbulence. So, it is unusual to find this type of installations either in urban or rural environments, as small scale wind infrastructures are still less convenient than micro-generation installations of solar power.

The present research describes and analyzes numerically the generation of electric energy by transforming the kinetic energy of an oscillating structure, induced by the vortex detachment as it is immersed in a fluid flow, commonly known as Vortex-Induced Vibrations (VIV). The structure to be analyzed is an inverted vertical cone coupled at the bottom to an elastic bar to which it is anchored, while it leaves the other end free to oscillate. The alternating detachment of the vortices over each side of the cone generates forces in a direction perpendicular to that of the stream flow, with equal frequency as the vortex shedding. These forces generate an angular oscillation of the whole structure, with respect to the anchor point of the elastic rod, which is maximized when the vortex detachment comes into resonance with the natural frequency of the structure.

There is an actual project already in development, designed by a Spanish startup company named "Vortex Bladeless", that introduces a VIV generation system like the one described here. The project still has not completed a research and simulation stage, although the generalities of the system are

already tested. There are two different models being developed. One is aimed at generating 4 kW, which might be particularly useful for micro-generation projects (both in rural and urban environments), and another smaller model that generates 100 W. These small-scale devices could provide, for instance, the required energy for the measurement of potential environmental variables in places that are hard to reach or off the grid.

The generation of electrical power through VIV systems has been the focus of many research studies as it has proven to be a very promising technology. In this scenario, it could certainly be very useful to have a tool capable of simulating the operation of these devices in order to contribute to their design and optimization by measuring their power output, resistance, durability, etc. Having the chance to calibrate numerically many design properties in advance, prior to the prototyping stage, could save a lot of time and resources.

Today all organizations, products or processes, including energy conversion from renewable sources, have to measure their "carbon footprint". This is the amount of carbon emissions they produce by direct or indirect action. In the case of renewable energy, and regardless of their final aim, generation devices usually consume large amounts of energy during their research, material extraction, construction, installation and maintenance stages. These different processes also produce greenhouse gas (GHG) emissions that are released into the atmosphere, generating a certain carbon footprint that can be measured in equivalent carbon mass before producing any actual saving in environmental terms. However, these devices will eventually generate energy without producing emissions, or with much lower emissions than those emitted by conventional generators. In order to reach a balance in terms of efficiency, during their useful life these devices should make sure that the emissions avoided by producing clean energy surpass the emissions produced in the stages prior to its implementation. One of the great advantages of VIV systems, is that they have simpler and lighter materials and the installation and maintenance are much easier, which translates into a smaller carbon footprint and thus is easier to reach a positive balance.

On the other hand, the recent increase in the processing power of computers and the development of parallel computation have allowed to devise numerical models suitable for the simulation and resolution of flows in diverse conditions. In particular Computational Fluid Dynamics (CFD) codes played a crucial role, being able to explicitly solve the flow around obstacles and allowing to

capture the state of a certain specific situation. It is not surprising that the most advanced research projects, both academic and industrial, use CFD tools to achieve advances in a wide variety of subjects, with applications at every scale, from macro frames of reference for climate studies to micro-scales in the study of blood flows. There are also applications for these simulations in sports, design of transport systems, study of turbo-machines, dispersion of pollutants in urban environments, among many others. An accurate simulation may be a rather convenient way of producing useful data, mainly because of how cost-effective it is when compared with experiments performed in real, physical environments like flume tanks or wind tunnels. As the role of CFD is being expanded, more new applications will arise and so will the need to enhance the methodologies of simulation.

The Discrete Element Method (DEM) is well suited to represent both loosely elastic structures and flexible bodies, while the Finite Volume Method (FVM) is widely used to simulate fluid flow. In the last two decades, several open source fluid flow solvers have been made available under different grid topologies, ranging from fully structured, either orthogonal or not, through block-structured grids, all the way up to fully unstructured. Greater geometrical flexibility has been addressed also through the adoption of methods like Immersed Boundary Method (IBM) or local grid refinement.

Enclosed in this work there is a coupled model where the DEM method was implemented to represent the rod as a flexible body, the IBM was used to represent the mast, while the fluid flow was solved using caffa3d.MBRi, an open source fully implicit finite volume method for solving the 3D incompressible Navier-Stokes equations in complex geometry, presented by Usera et al. (2008).

1.2 Aims and objectives

The main objective of this work is to numerically represent the dynamics between a VIV energy collector device and a fluid flow, in this case a uniform air flow acting upon a vorticity wind turbine. The research seeks to obtain a qualitative representation of the movement and to quantitatively estimate the electric energy extracted by transforming the kinetic energy harvested in the oscillations.

A secondary objective of this work is to create a module for the caffa3d.MBRi where the DEM is coupled with the already existing FVM, so as

to create a tool capable of representing both elastic and flexible bodies, with the ability to transmit strain stress, compression and bending moment.

The VIV energy harvester is represented numerically using two methods: the elastic bar is modeled as a set of small bars with elastic bonds and bending moment transmission through the DEM, and the mast is determined using IBM. The flow dynamics are represented using the caffa3d.MBRi model, which also incorporates a simple linear generator model that describes a magnet oscillating along with the motion of the elastic bar, inducing emf in 3 fixed coils. The proposed study tool will be suited to the analysis of this type of structures, with a wide range of applications. Some examples of those potential applications could be the study of the effect of strong wind on electric transmission lines, the implementation of full aeroelastic numerical models for wind turbine blades and rotors, and the aero-elastic modeling of tension structures like hanging bridges, just to name a few.

In order to validate the developed tool, the coupled method was applied to the study of the dynamic of the cod end of a trawling fish net. An experimental computer model of a tunnel net was carried out, which was also contrasted with an experiment in the naval and maritime testing channel of the University, which qualitatively compared its results to the form previously adopted by the rig with fishing load in the simulation.

1.3 Research Flow

This research will be presented in five chapters, each of them containing a section dedicated to Vorticity Wind Turbine (VWT), as the main matter, and also a subsidiary section oriented to the study of fish net tunnels. These lasts parts were extracted from a previous work that is currently being revised by the reviewers of the Journal of Computers and Fluids. The decision to present the previous research coupled with the current work was based on the fact that most of the tools developed for the study of fishing nets were also used for the modeling of the VWT, but we had no physical test to measure the efficiency of the turbines in a field situation yet, as we did have for the fish net tunnel. Although the physical characteristics of both projects are diverse, the tools for the simulation of the variables are consistent, and can be used in both situations, having the back up of an already generated body of work in a physical environment that can be used to contrast the results.

A brief description of every chapter is given here:

- Chapter 1. Lists the motivations for studying the generation of electricity with VWT with both global and local perspectives. Outlines the purpose of the research with possible applications, analyze the current development of the technology and finally accounts the objectives of the research.
- Chapter 2. Makes a general review of the literature used in the research. It is divided in four main sections. First the state of the art of Vortex-Induced Vibrations (originally to avoid movement of structures) is presented and then with intention to favor the displacement and harvest energy. Also the fluid solver (caffa3D.MBRi) used for the research is described and the method for solving the movement of the turbine (DEM), which is coupled with the fluid flow solver in this research.
- Chapter 3. Presents a structural analysis of the vorticity wind turbine analyzing the effect of the wind acting over it. Secondly, the specific DEM algorithm is used for modeling the turbine and all its components, and also for modeling the fish net. And finally, there is a description of how the DEM and the FVM were coupled for solving the interaction between fluids and structures.
- Chapter 4. This chapter includes the application and 3D analysis of both models previously described. The results of the simulations are displayed along some figures and plots that provide quantitative and qualitative understanding of the dynamics of both systems.
- Chapter 5. The final chapter contains the conclusions reached in the research process and suggests some possible directions for further studies in the field.

Chapter 2

Literature Review

2.1 Vortex-Induced Vibrations

There are many research publications aimed to numerically predict the motion of structural VIV, most of them studying circular cylinders immersed in flowing fluids. It is well known that the flow around a fixed circular cylinder can be affected by a number of parameters, including Reynolds number, surface roughness, free stream turbulence level, etc. Likewise, when dimensional analysis is applied to elastically mounted cylinders there are also important variables to consider (listed in Table 2.1) related to their structural mass (m), structural damping (c) and stiffness (k = spring constant). These parameters are the most widely explored in the literature, but they are not the only ones that can be considered.

One of the first publications that presented considerable insight about VIV response of a cylinder was written by Parkinson (1972). He considered a mass, spring and dash-pot system driven by the fluid force resulting from vortex shedding. Equation (2.1) is the differential equation for transverse displacement (y) of a bluff body:

$$m\ddot{y} + c\dot{y} + ky = F_y = C_y \frac{1}{2}\rho_f V^2 D \tag{2.1}$$

where m = total oscillating structural mass; c = structural damping; k = spring constant; F_y = fluid force in the transverse direction; and the dot symbol stands for differentiation with respect to physical time t. Parkinson made two important assumptions in his research, the first being that the force and response are sinusoidal with the same frequency (f) and secondly that the

Table 2.1: Non-dimensional groups for a elastically mounted cylinder. Here ρ_f = fluid density, D = cylinder diameter; L = cylinder length; ρ_m = cylinder density; c = structural damping; k = spring constant. The ideal added mass, m_A, is given by $m_A = C_A \cdot m_d$, where m_d is the displaced fluid mass and C_A is the potential added mass coefficient. ($C_A = 1.0$ for a cylinder). U = free-stream velocity; A = transverse displacement amplitude. The frequency ratio f^* is defined as (f/f_{N_o}), where f is the oscillation frequency, and f_N is the natural frequency in the presence of fluid. F_y = transverse fluid force; μ = fluid viscosity and f_v = vortex shedding frequency.

Mass ratio	m^*	$\frac{m}{\pi \cdot \rho_f \cdot D^2 \cdot \frac{L}{4}} = \frac{\rho_m}{\rho_f}$
Damping ratio	ξ	$\frac{c}{2\sqrt{k \cdot (m + m_A)}}$
Mass-damping parameter	α	$(m^* + C_A) \cdot \xi$
Velocity ratio	U^*	$\frac{U}{f_N \cdot D}$
Amplitude ratio	A^*	$\frac{A}{D}$
Frequency ratio	f^*	$\frac{f}{f_N}$
Transverse force coefficient	C_Y	$\frac{F_y}{\frac{1}{2} \cdot \rho_f \cdot U^2 \cdot D \cdot L}$
Reynolds number	Re	$\frac{\rho_f \cdot U \cdot D}{\mu}$
Strouhal number	St	$\frac{f_v \cdot L}{U}$

fluid force leads the response by a constant phase angle Φ, this is the so-called lock-in effect,

$$F_y(t) = F_{y_o} \sin(\omega t + \Phi) \tag{2.2}$$

$$y(t) = A \sin(\omega t) \tag{2.3}$$

where $\omega = 2\pi f$; f = oscillation frequency and A = amplitude of the oscillation. With these considerations and applying it to a flexible cylinder he obtained relations for the vibration amplitude, Eq. (2.4), and frequency, Eq. (2.5), as functions of the previous parameters, where the importance of the phase angle

and the role played by mass and damping (mass-damping parameter, α) was shown very clearly.

$$A^* = \frac{1}{4\pi^3} \frac{C_y \cdot \sin(\Phi)}{(m^* + C_A) \cdot \xi} \left(\frac{U^*}{f^*}\right)^2 \cdot f^* \tag{2.4}$$

$$f^* = \sqrt{\frac{(m^* + C_A)}{(m^* + C_{EA})}} \tag{2.5}$$

Here C_A is the potential flow added mass coefficient and C_{EA} is an "effective" added mass coefficient that includes an apparent effect due to the total transverse fluid force in phase with the body acceleration.

Since the research by Perkinson, several other studies have emerged that analyze changes induced in the response of a cylinder under VIV by varying the parameters previously described. Griffin et al. (1975) made the so-called 'Griffin plot', where the maximum VIV amplitude was plotted against the Shop-Griffin parameter, $S_G = 2\pi^3 St^2 (m^* \xi)$, and it was believed for some time that the amplitude of the VIV is insensitive to Reynolds number changes. However, Klamo et al. (2005) and Govardhan and Williamson (2006) have both since demonstrated the strong influence of the Reynolds number on the maximum VIV amplitude of a cylinder, and in the latter it is proposed that the amplitude is given by $A^* = g(\alpha) \cdot f(Re)$ presented in Eq. (2.6). Refer to Williamson and Govardhan (2008); Bearman (2011) for more detailed reviews.

$$A^* = \left(1 - 1.12\,\alpha + 0.30\,\alpha^2\right) \log\left(0.41\,Re^{0.36}\right) \tag{2.6}$$

For the purposes of the current research, and apart from a comprehensive review of the state of the art in the academic literature, some specific practical tools devised for the industry have been used as a conceptual reference. There is a very complete set of parameters requested by the *Guide for the assessment of wind actions and effects on structures* from the Advisory Committee on Technical Recommendations for Construction (2010), in Italy, to be included in the standard documentation of limitations and requirements to civil engineering structures related to wind actions (pressure, forces, moments, etc.), a model that deals with the overall resistance of structures and their subsidiary components, including both structural and non-structural elements. The documentation also includes some explicit examples of application to different kinds of structure. Such line of inquiry, once adapted to a slender

structure, could be directly applicable to the VWT being studied in this work, and for that reason it has been included into the research process.

The analysis for a slender structure starts by considering the actions in the along-wind direction. The second stage, and the most relevant for the current research, deals with the determination of the actions of critical wind velocities that may cause resonant vortex shedding with the structure vibration, in particular initial calculations concerning the critical wind velocities and the corresponding Scruton number, a dimensionless coefficient for the characterization of the response of structures due to the effect of wind loads, calculated as:

$$Sc = \frac{4\pi \cdot m_{e,1} \cdot \xi_s}{\rho_{air} \cdot D_{ref}^2} \tag{2.7}$$

where $m_{e,1}$= equivalent mass per unit length, ξ_s = structural damping and D_{ref} = the reference diameter. Subsequently, two methods for determining the peak tip deflection are provided. In Section 3.1 this analysis is specifically applied to VWT.

The document provides a very precise explanation of the aero-elastic regime, mainly providing ways to avoid it, whereas in the case of the VWT the goal is exactly the opposite, as the vibration is at the core of the energy conversion process. In resonance conditions between the vortex shedding and the natural frequency of the structure, the smaller the Scruton number (and therefore the lighter and/or low damped the structure) the greater the response. In Figure 2.4a, the normalized standard deviation of the tip across-wind displacement is plotted as a function of the reduced mean velocity and parametric in Sc. When Sc is large, the across-wind response increases only moderately, within a small range around the critical velocity. For lower values of Sc, the across-wind response increases abruptly and the resonance extends to a much broader range of values of the wind velocity, mainly to higher values of velocity.

Figure 2.4b shows the maximum value of the normalized standard deviation of the across-wind response at the top of the structure as a function of the Scruton number. Two main regimes with a transition in between can be identified:

• For large values of Sc (usually higher than 30), vibrations are forced by vortex shedding and they have a random nature. Thus, the probability of lock-in is quite low and the load induced by the vortex shedding is not critical.

Figure 2.1: Transversal response for large values of Sc

• For intermediate Sc values (from 5 to 30), a transition occurs between the two types of behavior and vibrations have a hybrid nature. In this regime, the vortex shedding phenomenon is very sensitive to different parameters, first and foremostly the turbulence intensity.

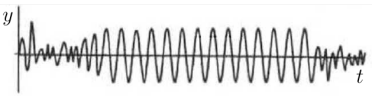

Figure 2.2: Transversal response for intermediate values of Sc

• For small Sc values (less than 5), vibrations are self-excited. The vortex wake produces vibrations of such an amplitude that they themselves trigger the shedding of vortices. Both the structure vibration and the vortex detachment have deterministic characteristics. This phenomenon is commonly known as the lock-in effect. In this regime, vibrations induced by vortex shedding may be very large.

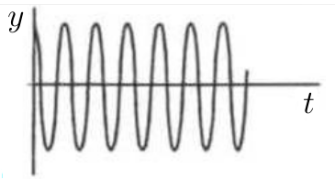

Figure 2.3: Transversal response for small values of Sc

This last regime is also called the aero-elastic regime. On Section 3.1 these calculations will be presented in detail, showing how these VWT can be designed to perform efficiently in this regime.

2.2 Harvesting Energy from VIV

Whilst the norm is to avoid such synchronization regimes (ie. analyzing the effect on buildings, bridges, etc.), the aim of this research is to examine the opposite: finding ways of promoting the vortex-induced vibrations of a bluff body in fluid flows, with the perspective of facilitating renewable energy production.

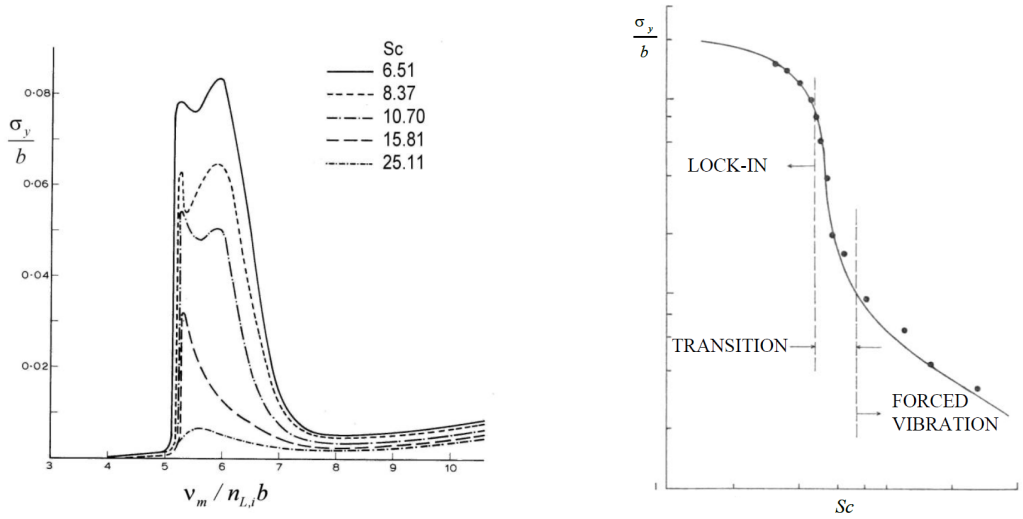

(a) Across wind response to vortex shedding parametric in Sc

(b) Domains of the across-wind response to vortes shedding

Figure 2.4: Across wind response to vortex shedding, figures taken from the *Guide for the assessment of wind actions and effects on structures*, Advisory Committee on Technical Recommendations for Construction (2010)

Electrical energy can be produced if the oscillation of the cylinder periodically displaces a magnet inside a coil. The energy production device will induce a structural damping term in the equation governing the motion of the cylinder, the underlying idea being that the energy dissipated by structural damping is at disposal to be harvested. Such an approach is physically tractable and has many potentially practical applications.

There are already many works aimed at the conversion of hydro-kinetic energy into a usable form of energy by enhancing the VIV of cylinders. Bernitsas et al. (2008b,a) introduce the Vortex-Induced Vibrations Aquatic Clean Energy (VIVACE) converter, where a rigid VIVACE cylinder at high damping and Reynolds number, is supported by a two linear springs system, a system damping c_{system}, transmission mechanism damping c_{tra}, a generator with damping c_{gen}, and the energy harnessing damping c_{harn}. The cylinder is placed with its axis in the $z-$direction perpendicular to the flow velocity U, which is in the $x-$direction. The cylinder oscillates in the $y-$direction, which is perpendicular to its axis in z and the flow velocity in x. The research presents the experimental results from a laboratory rig where a variable electrical load resistance was connected to optimize the harnessed energy, reaching an integrated power efficiency of $\eta_{vivace} = 0.22$ and a peak of $\eta_{peak} = 0.31$.

Barrero-Gil et al. (2012) had an interesting efficiency approach. Knowing that the energy transfer can be quantified in terms of work done per unit length by the fluid over one cycle of oscillation (T), then it is possible to introduce the efficiency η defined by the ratio of the mean power imparted by the flow to the body per unit length P_{F-B} and the total power resulting in the flow per unit length P_F.

$$\eta = \frac{P_{F-B}}{P_F} \tag{2.8}$$

where the total power in the flow per unit length is $\rho U^3 D/2$. The power extracted from the flow by the oscillating body, per cycle of oscillation and per unit length, is given by

$$P_{F-B} = \frac{1}{T} \int_0^T F_y \, \dot{y} \, dt \tag{2.9}$$

Considering a steady state of sinusoidal oscillations with amplitude "A" and frequency "f" it follows from Eq. (2.4) and Eq. (2.8) that the conversion factor can be expressed in terms of the normalized amplitude, normalized velocity, normalized frequency, and the fluid lift force excitation coefficient $C_Y \sin\Phi\left(\frac{f^*}{U^*}\right)$

$$\eta = \pi A^* C_Y \sin \Phi \cdot \left(\frac{f^*}{U^*}\right) \tag{2.10}$$

From Eq. (2.10), it can be seen that, for a particular Reynolds regime and fixed mechanical properties (m^* and ξ), computation of efficiency requires the fluid force coefficients ($C_Y \sin\Phi$ and $C_Y \cos\Phi$) as a function of the normalized amplitude of oscillation and the true reduced velocity $V^* = U^*/f^*$. Finally, it should be noted that the efficiency can also be defined considering the total area covered by the oscillation device during its motion. In that case,$\bar{\eta} = P_{F-B}/P_{F^*}$, where in the case of a elastically mounted cylinder $P_{F^*} = \rho U^3(2A + D)/2$.

In a recent publication, Soti et al. (2017) explores numerically the generation of electrical power from VIV on a cylinder. In their work, the cylinder is free to oscillate in the transverse direction, attached to a magnet that can move along the axis of a coil made from conducting wire. The magnet and coil constitute a basic electrical generator and, according to Faraday's law of electromagnetic induction, the motion of the magnet produces a emf (ϵ) across the coil. If the coil is connected to a resistive load, an induced current will counteract the motion of the magnet by applying electromagnetic force.

For the calculation of the electromagnetic force they use the single magnetic dipole approximation proposed by Donoso et al. (2010) that includes a mathematical model of the interaction between a $N - turns$ coil and a single oscillating magnet. A set of experiments that validates the theoretical model of the oscillator are also presented and discussed in the publication. The magnetic force opposing the movement of the magnet is provided by Eq. (2.11) where $c_{m0} = \mu_m^2/(RD^4)$ is a constant (μ_m = magnetic moment of the magnet; R = resistive load; and D = diameter of the oscillating cylinder). And $g = g(y(t))$ is a function of the dimensions of the coil and its distance to the magnet, provided in Eq. (2.12).

$$F_m = c_{m0} \cdot g^2 \cdot \dot{y} \tag{2.11}$$

$$g(y) = \frac{2\pi N a^2}{L}\left[\frac{1}{\left(a^2 + (y_{cm} - L/2)^2\right)^{3/2}} - \frac{1}{\left(a^2 + (y_{cm} + L/2)^2\right)^{3/2}}\right] \tag{2.12}$$

where y_{cm} = the distance between the magnet and the coil; a = diameter of the coil; L = length of the coil. The magnetic force can be considered as a damping force with a non-constant damping coefficient $c_m = c_{m0}g^2$. The electrical power is calculated by multiplying the electromagnetic force with the velocity of the magnet $P(t) = F_m\dot{y}$. Lastly the efficiency is defined as the ratio of the electrical power to the power available over the fluid region occupied by the cylinder (not considering the amplitude of the oscillation). Several results are presented comparing constant versus electro-magnetic damping ratio, varying the coil length, coil radius, mass ratio, Reynolds number and finally using two coils. In all cases a maximum average efficiency of $\eta = 0.13$ was obtained.

A recent publication from PRACE (Partnership for Advanced Computing in Europe), Cajas et al. (2016) includes research on a parallel multi-code coupling for simulating the physical response of a scaled model of the turbines proposed by the Spanish startup company, "Vortex Bladeless". The paper compares the results against experimental data from wind tunnel tests. In the publication, the authors explain that the research is limited to a first stage of the project, and that the interest for following lines of inquiry is to improve the efficiency code in order to simulate the full-scale wind energy generator and provide reliable energy production prediction for the device.

2.3 Computational Fluid Dynamics, CFD

In the last two decades several open source fluid flow solvers have been made available Zaleski (2001), under different grid topologies ranging from fully structured, either orthogonal or not Lehnhäuser and Schäfer (2003), through block-structured grids Lilek et al. (1997), and up to fully unstructured. Greater geometrical flexibility has been addressed also through the adoption of methods like local grid refinement Lange et al. (2002), and immersed boundary Liao et al. (2010); Mendina et al. (2014) atop the underlying grids. A detailed review of this last method, originally introduced by Peskin Peskin (1982), is given in Mittal and Iaccarino (2005a).

The Discrete Element Method (DEM) is well suited to represent freely moving bodies and loosely elastic structures, while the Finite Volume Method (FVM) is widely used to simulate fluid flow Ferziger and Peric (2002); Lehnhäuser and Schäfer (2002). In this work we present a coupled model where a simple DEM method is implemented to represent the elastic rod, while the fluid flow is solved using caffa3d.MBRi Usera et al. (2008); Mendina et al. (2014) an open source fully implicit finite volume method for the 3D incompressible Navier-Stokes equations in complex geometry.

2.3.1 Fluid Flow Solver

The open source fluid flow solver caffa3d.MBRi is used in this work. A brief presentation of the solver is given in this section, with further details and solver validation examples available in Usera et al. (2008); Mendina et al. (2014).

The caffa3d.MBRi solver follows the FVM in three dimensional block structured curvilinear grids. The underlying mathematical model comprises the mass balance equation, Eq. (2.13) and momentum balance equation, Eq. (2.14) for a viscous incompressible fluid, together with generic passive scalar transport equation, Eq. (2.15) for scalar field ϕ with diffusion coefficient Γ. Note that Eq. (2.14) has been written only for the first Cartesian direction here.

$$\int_S (\vec{v} \cdot \hat{n}_S) dS = 0 \tag{2.13}$$

$$\int_\Omega \rho \frac{\partial u}{\partial t} d\Omega + \int_S \rho u (\vec{v} \cdot \hat{n}_S) dS =$$

$$\int_{\Omega} \rho\beta(T - T_{ref})\vec{g} \cdot \hat{e}1 d\Omega + \int_{S} -p\hat{n}_S \cdot \hat{e}1 dS + \int_{S} (2\mu D \cdot \hat{n}_S) \cdot \hat{e}1 dS \quad (2.14)$$

$$\int_{\Omega} \rho \frac{\partial \phi}{\partial t} d\Omega + \int_{S} \rho\phi(\vec{v} \cdot \hat{n}_S) dS = \int_{S} \Gamma(\nabla\phi \cdot \hat{n}_S) dS \quad (2.15)$$

In these equations, $\vec{v} = (u, v, w)$ is the fluid velocity; ρ = fluid density; β = thermal expansion factor; T = fluid temperature; and T_{ref} = reference temperature; g = gravity, p = pressure, μ = dynamic viscosity of the fluid; and D = strain tensor. The balance equations are written for a region Ω, limited by a closed surface S, with outward pointing normal $\hat{n}_S$. Finally $\hat{e}1$ is the first Cartesian direction.

The generic transport equation, Eq. (2.15), for passive scalars can be used to implement in a straightforward manner further physical models like heat transport, turbulence models, etc. In this work the standard Smagorinsky Large Eddy Simulation (LES) turbulence model is used based on this scheme, Smagorinsky (1963).The use of equations in their global balance form together with the finite volume method, as opposed to the differential form, favors enforcing conservation properties for fundamental magnitudes as mass and momentum into the solving procedure Ferziger and Peric (2002).

The global grid is made up from structured grid blocks, which can be either orthogonal Cartesian grid blocks or curvilinear body fitted grid blocks. Nevertheless geometrical properties are always expressed in a Cartesian coordinate system, as well as flow properties which are expressed in primitive variables in the same Cartesian coordinate system, like velocities for example. To provide greater geometrical flexibility the immersed boundary method Liao et al. (2010) can be combined with both Cartesian and body fitted grid blocks.

Each equation in the mathematical model is discretized and linearized at each cell to obtain a discrete approximation in the form of Eq. (2.16), written again for the u velocity component, where the variable value at each cell center is related to the values at the six neighbors. Details for discretization of each term will not be given here but can be found in Usera et al. (2008), together with various validations of the solver Usera et al. (2008, 2006); Mendina et al. (2014).

$$A^u_P \cdot u_P + A^u_W \cdot u_W + A^u_E \cdot u_E + A^u_S \cdot u_S + A^u_N \cdot u_N + A^u_B \cdot u_B + A^u_T \cdot u_T = Q^u_P \quad (2.16)$$

A block structured variant of the Stone-SIP solver Lilek et al. (1997) solver

algorithm is used that accommodates well the block structure inherited from the grid, allowing efficient parallelization through Message Passing Interface (MPI).

To deal with the linearization and subsequent coupling of linear systems for each equation in the mathematical model, an outer-inner iteration scheme for each time step is employed, as shown in Eq. (2.5). Linear systems for each equation in the mathematical model are sequentially assembled and undergo inner iterations with SIP or AMG-SIP linear solvers. The outer loop is repeated within each time step until the desired level of convergence is achieved before continuing to the next time step.

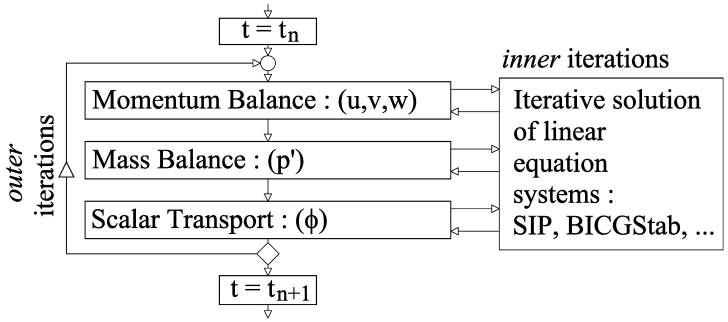

Figure 2.5: FVM iteration scheme for one time step (adapted from Ferziger and Peric (2002))

2.3.2 Immersed Boundary Method

The immersed boundary method is a natural alternative to body-fitted or unstructured-grid methods when the aim is to simulate flow in domains with complex rigid boundaries, such as in fluid-solid interaction problems, which generally results in larger requirements of memory and involves higher computational costs. This demand is not only increased by the requiring transient re-meshing strategies that further raises the computational overhead and algorithmic complexity of these approaches, but also because, as the grid gets deformed, it gets harder to maintain the efficiency in solving the associated governing equations discretized in the Cartesian grid.

The IBM not only has the advantage of keeping the structured Cartesian grids but also provides the possibility to handle more complex geometries. The method was first implemented by Peskin (1972), and then generalized in Peskin (2002), who replaced the boundary by a field force which is defined on

the mesh points of the rectangular domain and which is calculated from the configuration of the boundary. This numerical scheme was applied to the two-dimensional simulation of flow around the natural mitral valve (heart valve).

In an IBM the Navier-Stokes equations are discretized on a Cartesian grid and the boundary condition would be imposed indirectly through the modification of the momentum and continuity equations. In general, the modification takes the form of a source term (or forcing function, f_b) in the governing equations, that reproduces the effect of the boundary. These implementations can be performed in two different ways. The continuous forcing is characterized by including the forcing function into the continuous governing equations. This leads to two different forcing functions ($f_b = (f_m, f_p)$), one that deals with the momentum and the other one with the pressure. The equations are then discretized in a Cartesian grid. This method was used by Pesking in his research, using feedback forcing to drive the velocity at the boundary to rest. Although this method was formulated independently of the spatial discretization, which seems a promising feature, it can produce oscillations and is subject to severe stability constraints.

The second approach was proposed by Mohd-Yusof (1998), and it is commonly referred to as direct forcing or discrete forcing approach. Here the governing equations are first discretized on the Cartesian grid and then a forcing term (body force) is added in the source term, corresponding to the cells near the immersed boundary, in such a way that secures that the desired velocity distribution is satisfied at the boundary. This approach is sensitive to the discretization method. However, it provides easier control over numerical accuracy, stability and conservation properties of the solver. This approach was further extended by Fadlun et al. (2000), to reach a finite-difference formulation, where direct forcing was applied at the first Eulerian grid points external to the immersed boundary. Refer to Mittal and Iaccarino (2005b) for a further review and examples of the two approaches.

In the current work, the immersed boundary method is used, which it was already incorporated in caffa3d.MBRi. Refer to Mendina et al. (2014) for research that validates the method. Here it is used to model the mast of the VWT (see Section 3.2.1), represented as an inverted cone, using the direct forcing approach. It is also used to model the larger freely moving objects that correspond to the load in the simulations of the fish net tunnel, which are represented in that case as spheres. The right term on Eq. (2.16) is modified

at each time step for the cells inside the bodies or in their boundaries, in order to force the velocity to be the same than that of the object. Each geometrical object is represented mathematically, comprising several fluid flow grid cells across its volume. The resulting body force is integrated in the proximity of each object in order to compute the fluid force acting on it.

2.3.3 Discrete Element Method

The DEM is used for many kinds of applications. It is a numerical method for computing the motion and effects of a large number of small particles. As soon as computers became available, they started to be used for running physical simulations of the behavior of particles. With the advances in computing power and the development of numerical algorithms for nearest neighbor sorting, it has become increasingly possible to numerically simulate millions of particles on a single processor, and even more so with the rise of parallel computing.

The DEM was first used in applied physics for real-time modeling of plasma, semiconductors, liquids and phase-change simulations. A precondition for the appropriate use of the method is that the system to be represented should be rightfully interpreted as an assembly of objects, and the laws governing their interaction must be known in order to obtain meaningful results that could be consistent with reality. The early evolution of the method, as well as the theory and computational aspects of particle simulations are described in Hockney and Eastwood (1988).

In the field of rocks mechanics, a discontinuous analysis was first used by Cundall and Strack (1979). This work presents a developed full-scale computer program for analyzing discontinuous block assemblies in two and three dimensions. The method consists of deformable blocks and deformable contacts that become frictional contacts after failure. Since the publication by Cundall, many new applications to analyze fractures and large displacements of materials started to emerge.

Today DEM has become widely accepted as an effective method for addressing engineering problems in granular and discontinuous materials, especially in granular flows, powder mechanics, and rock mechanics. Nowadays its applications are being extended to analyze load and deformation on flexible and elastic systems in addition to the initial application for determining the failure of structures.

The general DEM is based on a double integration of the Newton equations of motion of each element. As the motion of an element is considered uncoupled from the motion of the rest of the elements during a time step, there is no need to assemble a stiffness matrix. Instead, coupling is obtained by updating the spring forces at every time step; each element will move, in the next step, due to the unbalance on the summation of forces in all springs attached to the element. Two types of damping are applied to reach equilibrium: the relative motion between elements of the structure is damped by a coefficient of damping calculated from the critical damping ratio of the material. Secondly, due to the motion of the structure immersed in fluid, there is a small amount of viscous damping, that represents the resistance of the medium in which the structure is placed.

Ivanov (2001), have developed a three dimensional DEM program for the analysis of engineering structures subject to earthquake loads. A chapter of his Ph.D. thesis is devoted to the analysis of shell structures with the DEM. In his work, he represents the in-plane stiffness of shells by a lattice of energy equivalent normal springs, while the bending stiffness of walls is represented by bending springs. He considers the elements of the lattice as beams that can transfer normal forces, F^n (due to tension and compression stresses), shear forces F^s, and bending moment M. In the research presented by Ivanov, the DEM algorithm to analyze solids is described in detail and used for the analysis of the shell structure. In Section 3.2.2 that algorithm will be adjusted to represent the dynamics of the flexible rod of the VWT.

DEM applied to Fish-Nets

The dynamic of fishing nets is a matter of high complexity, the fundamental reason being that the forces acting on these devices depend on their shape, and at the same time, due to the elastic nature of the materials that shape it, the form it adopts is strongly influenced by its interaction with the hydrodynamic flow and other forces. Being able to design and define the shapes that various types of fishing gear might acquire under different flow conditions, represents an important challenge in terms of energy, trading and sustainability. Improvements are needed in design configurations in order to achieve greater efficiency in fishing, allowing better gear selectivity and reducing also the hydrodynamic resistance to reduce fuel consumption Takagi et al. (2007).

There are many researches aimed at making changes in the construction of fish nets that help to improve the selectivity. Selectivity is the ability of the net to retain a target species and within it, individuals whose sizes are above the average size that define the maturity of the specimen. This ensures that young specimens can escape the device and continue to maintain the sustainability of the resource. And also ensures an improvement in the efficiency of the net from an economic standpoint and especially in environmental terms.

Several studies to numerically predict the configurations and loading acting on a fish net have been performed by various authors. Characterization of drag models for trawl bodies is performed in Balash et al. (2016) by means of extensive flume tank tests. Added mass affects are considered in Balash et al. (2009) for oscillating flows.

The design and setup of fishing nets can be aided by numerical simulations of their interaction during trawling with water and free bodies dragged by the stream, with the aim of predicting the shape adopted by the fishnet and the forces exerted onto it.

In Takagi et al. (2003, 2007); Shimizu et al. (2007) and Lee et al. (2005) the fish net is modeled as a system of lumped masses that are interconnected by springs without mass. The shape is estimated by calculating the displacements of these point masses under boundary and flow conditions assuming that moment is not transmitted between a mesh knot and a bar. A finite element approach is taken in Priour (1999, 2009) to optimize the energy performance of trawls design under uniform flow conditions.

To address the interaction between the fish-net and the flow, a coupled method is presented in Bi et al. (2014), with a lumped mass approach to model the fishnet and a porous-media model for the flow.

Chapter 3

Modeling

In this chapter the modeling of the VIV structure will be detailed. First a structural analysis as the one presented in the *Guide for the assessment of wind actions and effects on structures*, Advisory Committee on Technical Recommendations for Construction (2010) will be applied until reaching a value for the peak tip deflection. Secondly the computational modeling using DEM and its coupling with the fluid solver caffa3d.MBRi will be explored more thoroughly. As it was not possible to perform a physical test in wind tunnel of the VIV structure, Section 3.3 presents the modeling of a trawling fish net tunnel, similar to the one used in a physical test in a towing tank. Results and comparison are provided in chapter 4.

3.1 VIV - Structure Analysis

In this section the Technical recommendations for construction included in the *Guide for the assessment of wind actions and effects on structures* from the Advisory Committee on Technical Recommendations for Construction (2010) will be carried out to analyze the vorticity wind turbine (VWT). Note that the referenced document purpose was to study the stability of the analyzed structure, with recommendations intended to avoid larger displacements; this work is aimed at achieving exactly the opposite, seeking to maximize the resonance between the natural frequency of the structure and the vortex shedding.

Geometry of the structure

The VWT structure consists of four essential parts:

- **Foundation:** underground structure that adds stability to the turbine
- **Generation system:** the kinetic energy from the oscillations is converted into electricity by a built-in linear alternator.
- **Rod:** made of carbon fiber, it provides strength and flexibility to the movement, while minimizing energy dissipation and providing the highest resistance to fatigue. It penetrates into the mast for 20 percent of the mast length, is anchored to it at its top end and the bottom is secured to the foundation.
- **Mast:** light conic structure built using resins reinforced with carbon and glass fiber that oscillates. It is designed to be substantially rigid, remaining anchored to the rod at its bottom. The top is unconstrained and presents the maximum amplitude of the oscillation.

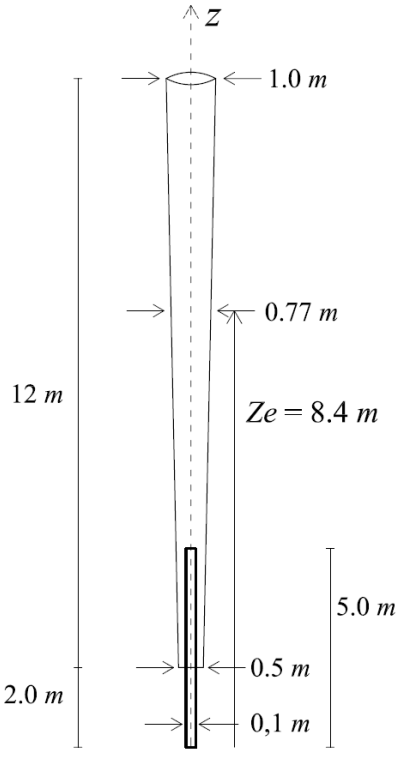

Figure 3.1: Scheme of the vorticity wind turbine

The mast is an axisymmetric body, of height $L_M = 12\,m.$, which is modeled by two functions ($f_1(z)$ and $f_2(z)$), represented as two parallel lines separated by

a distance that is equal to the thickness of the wall, $t = 2\,mm.$, rotated around axis z. These functions represent the distance from the external and internal surface to the symmetry axis z, respectively.

$$f_1(z) = 0.250 + \frac{1}{24}\,z \tag{3.1}$$

$$f_2(z) = 0.248 + \frac{1}{24}\,z \tag{3.2}$$

The rod is a cylinder of length L_r= 5.0 $m.$ and diameter $D_r = 0.1\,m.$, that penetrates 3 meters into the mast (25 % of L_M). In Fig. 3.1 there is a diagram of the structure, where z_e is the equivalent height ($z_e = 0.6 \cdot L_{tot}$), and here D_{ref}=$D_M(z = z_e) = 0.77\,m.$

Mass of the structure

To calculate the mass of the structure, a cylindrical coordinate system is used for the integration (z, r_z, θ), where r_z = distance from axis z; and θ = angle around axis z. An infinitesimal element of volume can be expressed as $dV = (dz)(dr_z)r_z(d\theta)$ and for the mass $dm = \rho(z, r_z, \theta)dV$. Thus, the differential of the mass can be calculated as:

$$dm = r_z\rho(dz)(dr_z)(d\theta) \tag{3.3}$$

integrating between $z_0 = 0$ and $z_f = L_m$:

$$m_{mast} = \int_{z_0}^{z_f} \left\{ \int_{f_1}^{f_2} \int_0^{2\pi} \rho_{mast}\, r_z\, d\theta\, dr_z \right\} dz \tag{3.4}$$

solving the integral with $\rho_{mast} = 845\,kg/m^3$ the mass of the mast is $m = 63.6\,kg$. The mass of the rod is calculated as the product of the volume by its density $\rho_{rod} = 1600\,kg/m^3$,

$$m_{rod} = \rho_{rod} \cdot V_{rod} = 1600\,\frac{\pi \cdot 0.10^2}{4}\,5 = 62.8\,kg \tag{3.5}$$

and so, the total mass is given by adding the rod and mast mass, $m_{tot} = m_{rod} + m_{mast} = 126.4\,kg$

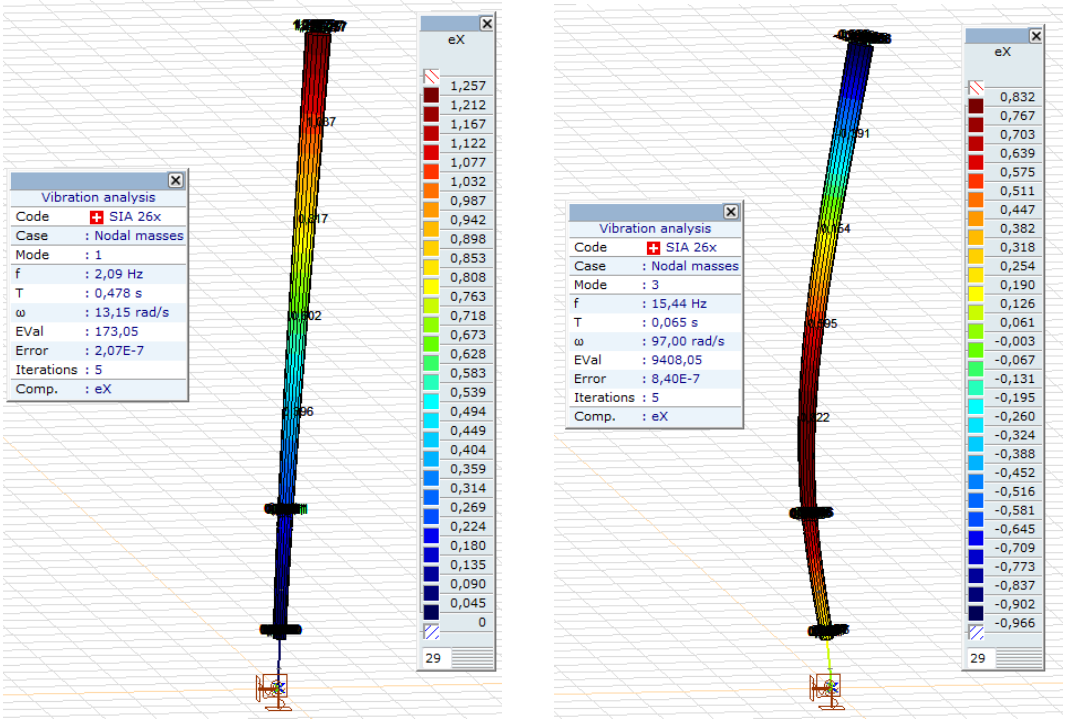

(a) First and second vibration modes **(b)** Third and fourth vibration modes

Figure 3.2: Schemes of the vibrations modes analysis using *AxisVM13*.

Finite Element Analysis

Due to the complexity of the structure, the bending natural frequencies, for the first and second mode shapes of the structure (f_N), are calculated using the software *AxisVM*, a finite element structural analysis software. Figure 3.2a shows the analysis for the first and second vibration modes, and Fig. 3.2b shows the third and fourth modes. As the structure presents polar symmetry, the vibration modes occur in pairs. This means that the first and the second vibration are equivalent, and also the third and fourth. The natural frequencies can be calculated using the software:

$$f_{N1} = f_{N2} = 2.09\,Hz \tag{3.6a}$$

$$f_{N3} = f_{N4} = 15.44\,Hz \tag{3.6b}$$

Generalized and Equivalent Mass

The following calculations are limited only to the first vibration mode $\Phi_1(z)$, because the interest here is to verify the oscillations in this specific mode. According to the literature, the generalized mass of the structure, m_1, is given by Eq. (3.7).

$$m_1 = \int_0^L m(z) \cdot \Phi_1^2(z) \cdot dz \tag{3.7}$$

where $m(z)$ is the mass per unit length, and L is the height of the structure. And the equivalent mass per unit length, $m_{e,1}$ is given by Eq. (3.8).

$$m_{e,1} = \frac{m_1}{\int_0^L \Phi_1^2(z) \cdot dz} \tag{3.8}$$

To solve Eqs. (3.7) and (3.8) the structure is divided in 14 equal parts of $dz = 1\,m.$, and simulated in the software AxisVM to obtain the value of $\Phi_1(z)$. The mass per unit length of the rod is directly calculated with Eq. (3.5); and the mass of the mast per unit length is obtained by changing the integration limits in Eq. (3.4). Table 3.1 shows the calculations required to obtain m_1 and $m_{e,1}$. Adding up the sixth column the generalized mass is obtained, and then dividing that result by the sum of the last column, the equivalent mass is obtained.

$$m_1 = 55.0\,kg \tag{3.9}$$

$$m_{e,1} = \frac{55.0}{8.12} = 6.78\,\frac{kg}{m} \tag{3.10}$$

Actions due to Vortex Shedding

To calculate the equivalent static actions associated with vortex shedding, it is necessary to determine first the critical velocities, that is the mean wind velocity that gives rise to the resonance condition (f_{vs}=f_N), and the relative Scruton number. Using Eq. (3.11) with $f_{N1} = f_{N2} = 2.09$, the across wind natural frequency of the structure in the fluid, for the first and second modes shapes, which are obtained from the finite element analysis. Evaluating where the mode shape is maximum (top according to Table 3.1), thus $D = D_{top} = 1\,m.$ and obtaining the Strouhal number as function of Reynolds number from

Table 3.1: Calculations to obtain the generalized and equivalent mass for the first vibration mode shape.

z $[m]$	$m_{rod}(z)$ $[kg/m]$	$m_{mast}(z)$ $[kg/m]$	$m_{tot}(z)$ $[kg/m]$	$\Phi_1(z)$	$m(z)\cdot\Phi_1^2(z)$ $[kg/m]$	$\Phi_1^2(z)$
1	12.56	0	12.56	0.030	0.0113	0.0009
2	12.56	0	12.56	0.090	0.102	0.0081
3	12.56	2.87	15.43	0.115	0.204	0.0132
4	12.56	3.30	15.86	0.237	0.891	0.0561
5	12.56	3.75	16.31	0.329	1.765	0.108
6	0	4.19	4.19	0.438	0.804	0.192
7	0	4.64	4.64	0.587	1.597	0.345
8	0	5.08	5.08	0.720	2.632	0.518
9	0	5.52	5.52	0.817	3.685	0.667
10	0	5.96	5.96	0.911	4.948	0.830
11	0	6.41	6.41	1.037	6.888	1.075
12	0	6.85	6.85	1.143	8.945	1.306
13	0	7.29	7.29	1.192	10.358	1.420
14	0	7.73	7.73	1.257	12.217	1.580
					55.0	**8.12**

Fig. 3.3.

$$v_{cr1} = \frac{f_{N1} \cdot D_{top}}{St} \tag{3.11}$$

With an iterative procedure, the critical velocity for the first and second modes shapes, which are the same due to the cylindrical symmetry of the structure, is obtained:

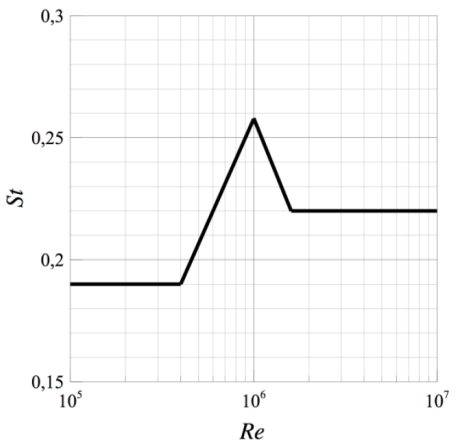

Figure 3.3: Strohual number for cylinders as a function of Reynolds number

Setting the Strouhal number to St= 0.23 and using $f_{N1} = 2.09$ (from Fig. 3.2a), the critical velocity can be calculated, then the Reynolds number and finally obtain St from Fig. 3.3, until convergence is reached:

$$f_{N1} = \frac{St \cdot v_m}{D_{top}} \tag{3.12}$$

$$v_{cr} = 9.1\, m/s \tag{3.13}$$

$$Re = \frac{D_{top} \cdot v_{cr}}{\nu} = 6 \times 10^5 \tag{3.14}$$

The convergence is achieved for a wind velocity of v_{cr}= 9.1 m/s, with this velocity at the top of the structure the Reynolds number is $Re = 6 \times 10^5$. Then the Scruton number is calculated with Eq. (3.15), where the structural damping is ξ_s= 0.008 for carbon fiber.

$$Sc = \frac{4\pi \cdot m_{e,1} \cdot \xi_s}{\rho_{air} \cdot D_{top}^2} = 0.57 \tag{3.15}$$

This is a very low value for the Scruton number, which means that the resonance conditions can be extended to a higher range of values of wind velocity, and the vibrations due to vortex shedding may be, as expected, very large.

For calculating the peak tip deflection, Eq. (3.16) to Eq. (3.24) are followed:

$$y_{pL} = g_L \cdot \sigma_L \tag{3.16}$$

where g_L is the peak deflection factor given by Eq. (3.17) and σ_L is the standard deviation of the deflection, heading Eq. (3.21). The peak deflection factor is a function of the Scruton number as follows:

$$g_L = \sqrt{2} \cdot \left\{ 1 + \left[Arctan\left(0.7 \cdot \left(\frac{Sc}{4\pi \cdot K_a} \right)^{2.5} \right) \right]^{1.4} \right\} \tag{3.17}$$

here, K_a is the dimensionless aerodynamic damping parameter, given by Eq. (3.18), with $K_{a,max}$ as the maximum value of the aerodynamic damping parameter in the absence of turbulence in the air flow, corrected then by the turbulence factor, C_I, and associated with the critical vortex shedding in the first mode.

$$K_a = K_{a,max} \cdot C_I \tag{3.18}$$

$$K_{a,max} = 5.075 - 0.715 \cdot \log Re \tag{3.19}$$

$$C_I = 1.3 - 0.06 \cdot v_{cr} \tag{3.20}$$

The normalized standard deviation of the deflection is given in Eq. (3.21) where c_1 and c_2 are dimensionless coefficients resulting from Eq. (3.22) and

Eq. (3.23) respectively.

$$\frac{\sigma_L}{D_{top}} = \sqrt{c_1 + \sqrt{c_1^2 + c_2}} \tag{3.21}$$

$$c_1 = \frac{a_L^2}{2}\left(1 - \frac{Sc}{4\pi \cdot K_a}\right) \tag{3.22}$$

$$c_2 = \frac{a_L^2}{K_a}\frac{\rho \cdot {D_{top}}^3}{m_e \cdot L}\frac{C_c^2}{St^4} \tag{3.23}$$

Where a_L is the normalized limiting amplitude, here the amplitude of the oscillation is sought to be similar to the diameter, thus $a_L = 1$. Lastly, C_c is a dimensionless parameter, function of the shape of the cross section and the Reynolds number, for circular cross section it is given by Eq. (3.24).

$$C_c = 0.07 - 0.01 \cdot \log Re \tag{3.24}$$

and finally the amplitude of the oscillation at its top end is obtained,

$$y_{pL} = 1.38\, m \tag{3.25}$$

3.2 VIV - Computational Modeling

The strategy to analyze the VWT structure is to divide it in two main parts, the rod and the mast, and treat the forces acting over these parts separately. The rod is analyzed as a beam anchored vertically to the ground with the DEM method, while the mast is represented by the Immersed Boundary Method.

The domain for the simulations is presented as a prism of $(8 \times 6 \times 15)$ meters in the (x, y and z) directions respectively. It is divided in cubic cells of $5\, cm$ side distributed in four blocks and regions of $(2 \times 6 \times 15)$ meters, one block for each region, named as blocks I, II, III and IV from west to east (x direction). The western block of the domain, block I, has inlet boundary condition where a uniform flow of $U_o = 9.1\, m/s$ in the x direction enters to the domain by its west boundary, the east boundary of this block has interface boundary conditions as the middle blocks, II and III, in their west and east boundaries and the eastern block, IV, in its west boundary. Block IV, has null-gradient outlet boundary condition in its east boundary. All, north, south, top and bottom boundaries of the four blocks have non-slip walls boundary conditions.

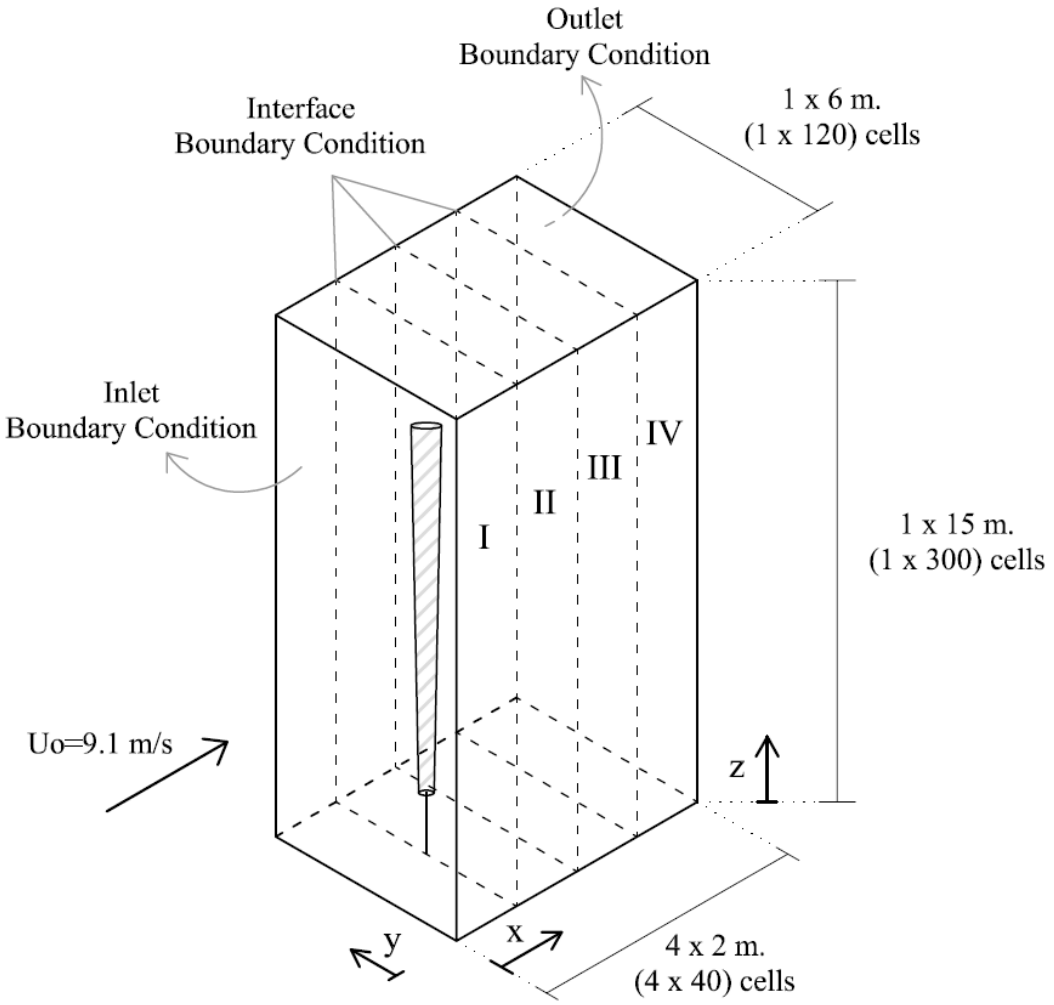

Figure 3.4: Domain scheme for the VWT simulation

A processor is used for each region, and so four processors (Xeon E5 family at Cluster-fing) are used for the simulations with MPI, parallel computing. Thus, the whole domain consists of $(160 \times 120 \times 300)$ cells adding a total of 5,760,000 cells, 1,440,000 computed in each processor. The time step for the fluid flow solver is set at $dt = 0.01\,sec$ and for computing 1 second of simulation time it takes almost one hours of computing time.

Besides the domain seems to be too short and narrow, a bigger domain simulation ,$(16 \times 9 \times 15)$ meters, was carried through and the behavior of the VWT was comparable to that from the smaller domain simulations, with no more than 10% in the variation of the results. So it was decided to provide the small domain results because of the savings in time and resources for every change implemented in the simulations.

3.2.1 Mast

The mast is an inverted cone as shown in Fig. 3.1, represented as a rigid structure with the direct forcing approach of the IBM introduced in Section 2.3.2. It is represented mathematically at each time step as a function of the position and normal direction of the last element of the rod (described in Section 3.2.2).

The source term, Q_P^u in Eq. (2.16), corresponding to the cells inside of the mast, is modified to make the velocity of each cell equal to the translational velocity of the mast. This is equivalent to adding a mass field $\vec{F^*}$ in the inner cells. Integrating this field in a closed region (D) surrounding the mast, the force that the body exerts over the fluid is obtained, and so:

$$F_{imb} = -\int_D \rho\, \vec{F^*}\, dV \tag{3.26}$$

the same can be applied to calculate the moment that the overall force exerts over the connecting node (CN) of the elastic rod, this the highest node of the rod, where the mast and the rod are connected.

$$M_{imb} = -\int_D (P - O) \wedge (\rho\, \vec{F^*})\, dV \tag{3.27}$$

Where $(P - O)$ is the distance from every computing point from the region (D) to the connecting node. Once the force that the fluid exerts over the mast (F_{imb}) and the moment with respect to the connecting node (M_{imb}) are calculated, the procedure continues with the analysis of the rod.

3.2.2 Rod

The rod is the main section for the modeling of the structure because of its flexibility and elasticity. It is constructed with the DEM approach proposed by Ivanov (2001), composed of 20 equal bars of length $l = 10\,cm$ and diameter $D_{rod} = 10\,cm$, that conform the 2 meters rod (L_{rod}), see Fig. 3.5a. Note that, as the mast is modeled with IBM as a rigid body, there is no bending taking place in the part of the rod that penetrates into the mast, and for that reason only the first two meters of the rod have to be modeled. Each bar is constructed as a linear bar with two punctual nodes, sharing with the next bar one of those punctual nodes at each end, schematic representation in Fig. 3.6b. The nodes are the points in which the forces and moments are transmitted from bar to

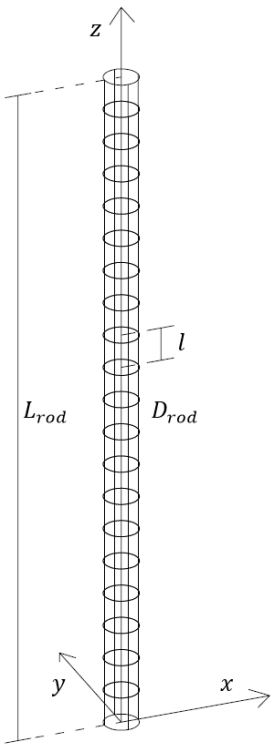

(a) Rod DEM Scheme

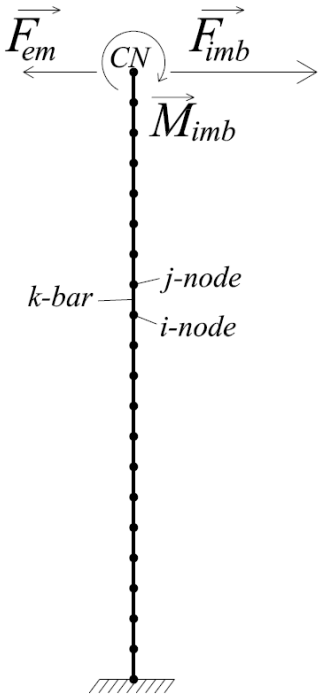

(b) Scheme of the modeling of the rod with the immersed boundary force and moment, and the magnetic force applied over the connecting node.

Figure 3.5: Modeling of the Rod

bar. Figure 3.6 shows the schematic representation of forces in Fig. 3.6a and the corresponding deformations in Fig. 3.6b, the bar is named with a counter "k" (from 1 to 20) and the nodes are marked with the subindex's "i" and "j". The external forces, and moment are applied in the highest node, named as "Connecting-Node" (CN) because is the one that connects the rod and the mast.

The motion of each element of the rod is represented by the first and second cardinal equations, applied at the center of the bars and used to calculate the displacement and rotation of the nodes (endings). The first, Eq. (3.28), is the equation for translational motion, and the second for rotational motion, Eq. (3.29), of a single element "i".

$$\ddot{x}_i + \alpha\,\dot{x}_i = \frac{F_i}{m_i} + g \tag{3.28}$$

$$\dot{\omega}_i + \alpha\,\omega_i = \frac{M_i}{I_i} \tag{3.29}$$

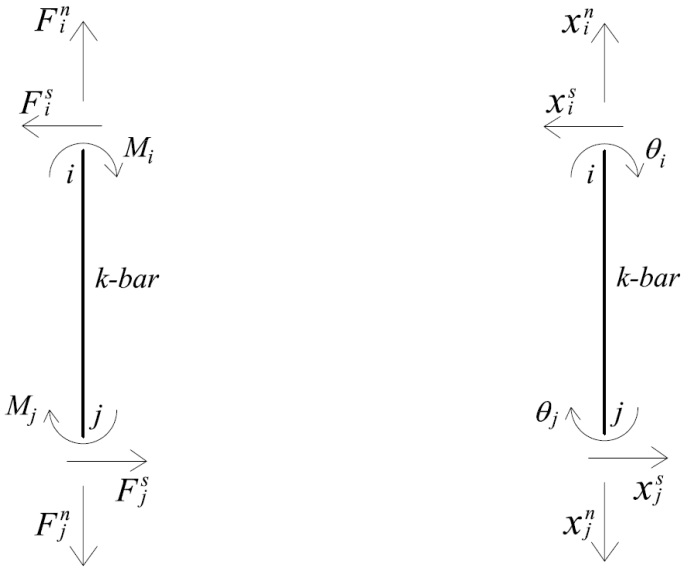

(a) Schematic representation of forces acting over each bar

(b) Schematic representation of deformations of the bars

Figure 3.6: Forces and deformations of the bars

where x_i = position vector; ω_i = rotational velocity; m_i = mass; I_i = mass moment of inertia; and g = gravity acceleration. The dots represent the derivative in time. A centered finite difference is used for the integration of the equations of motion. New and old values, within a time step, are designated by superscripts plus and minus respectively, thus the expression for translational and rotational velocities are provided by

$$\dot{x}_i = \frac{1}{2}\left[\dot{x}_i^- + \dot{x}_i^+\right] \tag{3.30}$$

$$\omega_i = \frac{1}{2}\left[\omega_i^- + \omega_i^+\right] \tag{3.31}$$

and the expression for translational and rotational accelerations,

$$\ddot{x}_i = \frac{1}{\Delta t_{dem}}\left[\dot{x}_i^+ - \dot{x}_i^-\right] \tag{3.32}$$

$$\dot{\omega}_i = \frac{1}{\Delta t_{dem}}\left[\omega_i^+ - \omega_i^-\right] \tag{3.33}$$

inserting this expressions in the equations of motion, Eq. (3.28) and Eq. (3.29),

and solving for new values of velocities results in:

$$\dot{x}_i^+ = \left[D_1 \, \dot{x}_i^- + \left(\frac{F_i}{m_i} + g\right) \Delta t_{dem} \right] D_2 \tag{3.34}$$

$$\omega_i^+ = \left[D_1 \, \omega_i^- + \left(\frac{M_i}{I_i}\right) \Delta t_{dem} \right] D_2 \tag{3.35}$$

where $D_1 = 1 - (\alpha \, \Delta t_{dem}/2)$, and $D_2 = 1/[1 + (\alpha \, \Delta t_{dem}/2)]$, with $\Delta t_{dem} =$ time step for the DEM. The time step used for the displacement of the rod is smaller than the time step used by the fluid solver (caffa3d.MBRi), as the differential equations system governing the motion of the rod is too stiff, because of the high Young's module of the material, and then it is necessary to use a smaller time step than the one required for solving the fluid. In the simulations presented in this work, for every time step of the fluid solver the DEM is executed 10,000 times in order to reach the convergence of the system.

With the new velocities obtained, it is possible to update the contact forces in between bars, which depend on the properties of the system. To update the normal and shear forces, and bending moment, first the incremental displacements of the contact point due to translational and rotational motions of the elements are computed using the new values of velocities. Note that for each $k - bar$ there are two nodes (one at each end) denoted as 'i' and 'j'.

$$\Delta x_{ci}^{tr} = \dot{x}_i^+ \Delta t \qquad \Delta x_{cj}^{tr} = \dot{x}_j^+ \Delta t \tag{3.36a}$$

$$\Delta x_{ci}^{rot} = ic^+ \times \Delta\theta_i \qquad \Delta x_{cj}^{rot} = -jc^+ \times \Delta\theta_j \tag{3.36b}$$

where ic^+ and jc^+ are the current vectors from the center of the bar to the contact points, and $\Delta\theta_i$ and $\Delta\theta_j$ are the incremental rotation of the elements. For the first time step the method uses values of position and velocity provided as initial conditions. Thus, the total incremental displacement at the contact is:

$$\Delta x_c = (\Delta x_{cj}^{tr} - \Delta x_{ci}^{tr}) + (\Delta x_{ci}^{rot} - \Delta x_{cj}^{rot}) \tag{3.37}$$

which resolves into normal and shear components as:

$$\Delta x_c^n = (\Delta x_c \cdot n_{ij}^{+\prime}) \, n_{ij}^+ \tag{3.38}$$

$$\Delta x_c^s = \Delta x_c - \Delta x_c^n \tag{3.39}$$

here n_{ij} is the unit normal vector pointing from node "i" to node "j"; the

supra-index "′" stands for the transposed vector (so as to be able to calculate the product). And the angular displacements for nodes "i" and "j" can be calculated as:

$$\Delta\theta_i = \omega_i^+ \cdot \Delta\, t, \quad \Delta\theta_j = \omega_j^+ \cdot \Delta\, t, \tag{3.40}$$

then, the increment of force in the normal spring is expressed in Eq. (3.41), where A_t = transversal area; E = Young's modulus; l = element length; and ν = Poisson's ratio (material property).

$$\Delta F_c^n = k_n\, \Delta x_c^n, \quad \text{with} \quad k_n = \frac{\sqrt{3}}{3}\frac{A_t\, E}{l \cdot (1-\nu)} \tag{3.41}$$

The calculation of the increments of the shear force and bending moment is not as simple as the normal force and further calculations are needed. The relation between these forces and the corresponding displacement for the end-point i of the element 'k' with second moment of inertia I_k is expressed in Eq. (3.42) and Eq. (3.43),

$$F_i^s = \frac{12EI_k}{l^3}(x_i^s - x_j^s) - \frac{6EI_k}{l^2}(\theta_i - \theta_j) \tag{3.42}$$

$$M_i = \frac{6EI_k}{l^2}(x_i^s - x_j^s) - \frac{4EI_k}{l}\big(\theta_i - \frac{\theta_j}{2}\big) \tag{3.43}$$

with symmetric relations for node j, where x = position vector and θ = rotation of the element, see Fig. 3.6b. An additional set of spring constants is defined accounting for the bending behavior equal to the coefficients of Eq. (3.42) and Eq. (3.43) as follows: $k_{qq} = 12EI/l^3$, $k_{qm} = k_{mq} = 6EI/l^2$ and $k_{mm} = 4EI/l$. Then the respective contributions to the driving force and driving moment are calculated as functions of the relative incremental shear displacement Δx_c^s, and the incremental rotations of the elements $\Delta\theta_i$ and $\Delta\theta_j$.

$$\Delta F_i^s = -\Delta F_j^s = k_{qq}\Delta x_c^s + k_{qm} \cdot n_{ij}^+ \times (\Delta\theta_i + \Delta\theta_j) \tag{3.44}$$

Before incrementing the values of the contact forces, their old directions have to be corrected in order to reflect the latest orientation of the contact plane. The old normal force should be modified to be collinear to the latest unit normal vector,

$$F_c^{n-} = (F_c^{n-} \cdot n_{ij}^{+\prime}) \cdot n_{ij}^+ \tag{3.45}$$

The shear contact force is first updated to be co-planar with the latest contact

plane,

$$F_c^{s-} = a^+ \cdot (a^- \cdot F_c^{s-\prime}) + b \cdot (b \cdot F_c^{s-\prime}) \tag{3.46}$$

where a^+, a^- and b are auxiliary unit vectors given by the expressions $b = (n_{ij}^- \times n_{ij}^+)/|(n_{ij}^- \times n_{ij}^+)|$; $a^- = b \times n_{ij}^-$ and $a^+ = b \times n_{ij}^+$. Finally, the rotation of the contact shear force has to be considered along the n_{ij} axis. The average rotation along this axis will be $\Delta\theta = 1/2 \cdot (\Delta\theta_i + \Delta\theta_j) \cdot n_{ij}^{+\prime}$. The final updated old shear contact force (co-planar with the new contact plane) will be,

$$F_c^{s-} = \cos\Delta\theta \cdot F_c^{s-} + \sin\Delta\theta \cdot (a^+ \times F_c^{s-}) \tag{3.47}$$

once having corrected the direction of the old contact forces, the incremented ones will yield the new values, with $\Delta F_i^n = -\Delta F_j^n$ and $\Delta F_i^s = -\Delta F_j^s$,

$$F_i^{n+} = F_i^{n-} + \Delta F_i^n \qquad F_j^{n+} = F_j^{n-} + \Delta F_j^n \tag{3.48a}$$

$$F_i^{s+} = F_i^{s-} + \Delta F_i^s \qquad F_j^{s+} = F_j^{s-} + \Delta F_j^s \tag{3.48b}$$

Resuming Eq. (3.43), the increment of moments is computed as:

$$\Delta M_i = k_{qm}\, n_{ij}^+ \times \Delta x^s - k_{mm}\,(\Delta\theta_i + \Delta\theta_j/2) \tag{3.49}$$

$$\Delta M_j = k_{qm}\, n_{ij}^+ \times \Delta x^s - k_{mm}\,(\Delta\theta_j + \Delta\theta_i/2) \tag{3.50}$$

and the increment of the moment at both ends:

$$M_i^+ = M_i^- + \Delta M_i, \quad M_j^+ = M_j^- + \Delta M_j \tag{3.51}$$

This iterative procedure is computed for every bar composing the rod. When computing on the highest bar, the force that the fluid exerts over the mast (F_{imb}) is transmitted to the connecting node (the one that is connected to the mast), as well as the moment with respect to this node (M_{imb}), calculated in the previous Section 3.2.1 with the IBM. It should be also considered at this stage the magnetic force that the generator exerts over the rod (F_{em}), as it is also applied to the connecting node, see Fig. 3.6b. In the next Section 3.2.3, it will be explained how that magnetic force should be calculated.

$$F_{CN}^+ = F_{CN}^- + \Delta F_{CN} + F_{imb} + F_{em} \tag{3.52}$$

$$M_{CN}^+ = M_{CN}^- + \Delta M_{CN} + M_{imb} \tag{3.53}$$

Having computed the stresses and moment resultants acting on each element, the system is ready to enter a new time step. It is worth highlighting that as the time step for this procedure is smaller than the one for solving the fluid equations, the same immersed boundary force and moment are used during several iterations until the fluid solver time step is advanced.

3.2.3 Generator

The kinetic energy of the oscillations is converted into electricity using a linear built-in generator as the one described by Donoso et al. (2010). It is composed of a magnet coupled to the last bar of the rod, modeled as a punctual magnet, and two fixed coils, one at each side of the rod, see Fig. 3.7. When the system is oscillating, the magnet oscillates with the rod, generating an oscillating magnetic field inside the coils. According to Faraday's law of electromagnetic induction, the motion of the magnet produces emf (ϵ) across the coil. Connecting the coil to a resistive load, an induced current appears, opposing the motion of the magnet by applying an electromagnetic force (F_{em}), which can be considered as a damping force in the motion of the rod.

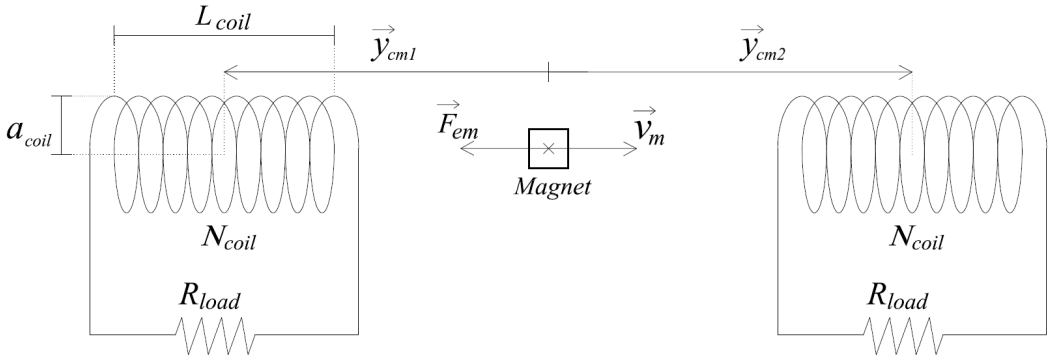

Figure 3.7: Scheme of the generator system

The magnetic force that each coil exerts over the magnet is a function of the magnet velocity and its relative position to the coils, as well as to the properties of the coils and the magnet, and the resistive load connected to each circuit. Here two identical coils are disposed at each side of the rod, connected to two identical loads for reaching a symmetrical displacement. In equilibrium conditions the center of the coils are located at 8.5 cm in $y-$ direction at each side of the magnet. The properties of the magnet and the coils are listed in

Table 3.2: Parameters used in the model of the generator

Property	Value	Unit
L_{coil}	7.0	cm
a_{coil}	5.0	cm
N_{coil}	700	turns
R_{load}	100	Ω
μ_m	4.5e-3	J/T
$y^0_{cm,1}$	-8.5	cm
$y^0_{cm,2}$	+8.5	cm

Table 3.2.

From the literature, the equation of the magnetic force ($F_{em,i}$) is obtained as follows:

$$F_{em,i} = c_{m0} \cdot g_i^2 \cdot \dot{y} \tag{3.54}$$

c_{m0} is calculated in Eq. (3.55), where μ_m is the magnetic moment of the magnet. Here it is constant because the resistive load (R) is set to be constant, but it could be variable, for instance, within the wind velocity.

$$c_{m0} = \frac{\mu_m^2}{R} \tag{3.55}$$

$g_i(y)$ is a function of the relative position between the $i-$coil and the magnet ($y_{cm,i}$), expressed as:

$$g_i(y) = \frac{2\pi N_{coil} a_{coil}^2}{L_{coil}} \cdot \left[\frac{1}{\left(a_{coil}^2 + (y_{cm,i} - L_{coil}/2)^2\right)^{3/2}} - \frac{1}{\left(a_{coil}^2 + (y_{cm,i} + L_{coil}/2)^2\right)^{3/2}} \right] \tag{3.56}$$

where the properties of the coil, denoted with the subindex "*coil*", are illustrated in Fig. 3.7, together with the distance from the magnet to each coil, $y_{cm,i}$.

The magnetic forces are calculated at each time step of the DEM, added in a single force (F_{em}), and applied to the highest bar of the rod as expressed in Eq. 3.52. Note that the magnet is also modeled as a punctual element. As this force opposes the motion of the bar and it is proportional to its velocity, it can be interpreted as a damping force.

To calculate the output power, P, the electromagnetic force is multiplied by the magnet velocity at each time step, the negative value is because the

force opposes the motion,

$$P(t) = -F_{em} \cdot v_{mg} \tag{3.57}$$

in this way, the output power is determinate just for an instant of time. Integrating the instantaneous power over a period of time T^*, the accumulated energy is obtained, and dividing then by the value of that period of time, the average output power, $\overline{P}$, is obtained:

$$\overline{P} = \frac{E_T}{T^*} = \frac{1}{T^*} \cdot \int_{T^*} P(t) \cdot dt \tag{3.58}$$

Finally, the efficiency of the VWT is defined as the ratio of the output power to the power available in the fluid flow over the region occupied by the turbine. The latter is constant in this simulations because an uniform flow is used. If dividing the instantaneous power, then the instantaneous efficiency is obtained, η; and the integrated efficiency, $\overline{\eta}$, is obtained dividing the integrated power:

$$\overline{\eta} = \frac{\overline{P}}{1/2\,\rho\, U^3 A_{VWT}} \tag{3.59}$$

Where U is the velocity of the fluid flow upstream, and A_{VWT} is the area occupied by the VWT in a plane perpendicular to the flow direction.

3.3 Fish Net Solver

The domain of this simulation is covered by one prism block with a length of $L = 4\,m$ in the principal direction of the flow (x direction) and a square section of size $a = 0.70\,m$ in y and z directions. The west boundary of the domain has inlet boundary condition where a uniform flow $U_o = 1\,{}^{m}/_{s}$ in the x direction enters to the domain. The east boundary is the outlet, and the rest of the boundaries, north, south, top and bottom are non-slip walls, although symmetry boundary conditions could also have been applied at these lateral boundaries. The discretization grid for the flow solver is made by cubic cells of $\Delta\, l = 0.01\,m$ length, totaling about 2 million cells. The properties of the fluid are assumed to be those of water. The time step for the flow solver is set to $dt = 0.01\,s$.

Here DEM is applied to represent the shape and stresses of a Fish Net

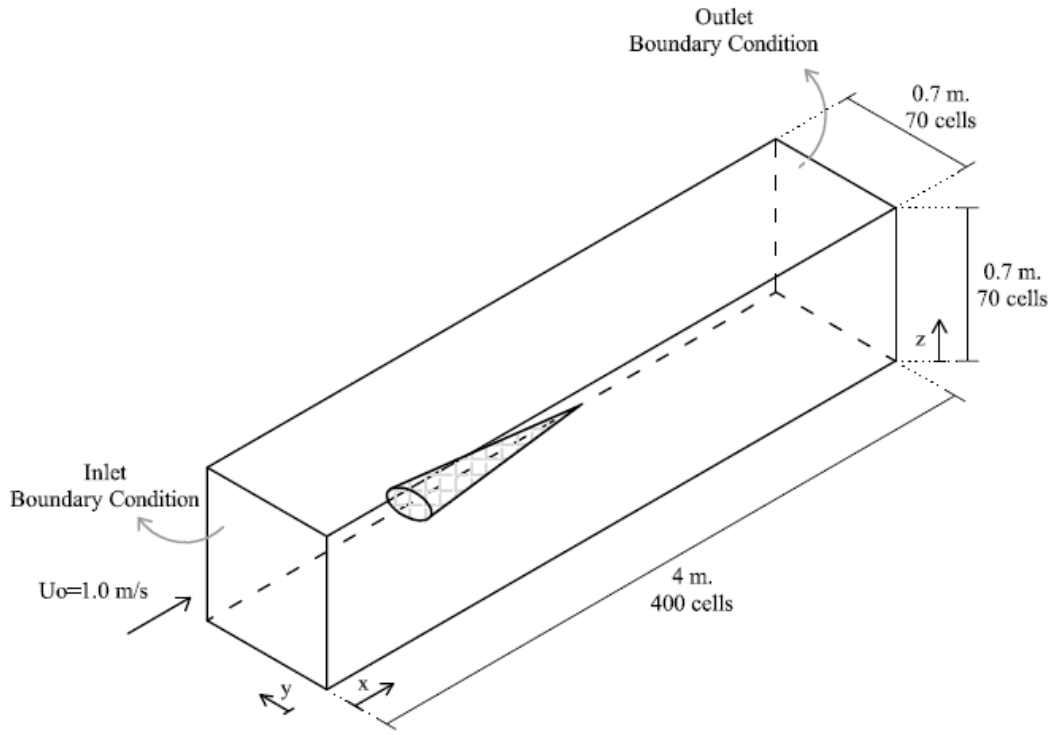

Figure 3.8: Domain for the Fish Net Tunnel simulation.

Tunnel in interaction with an axial stream of water and free bodies dragged by the stream. The results are then compared and validated with a Fish Net Tunnel trawled in a towing tank. The long term objective of the study is to develop a comprehensive model to simulate flexible bodies or elastic systems in interaction with fluids as a complementary tool to tank or wind tunnel testing.

The lumped masses model, with spring connections, is adopted in this work to model the Fishnet, similar to the previously referenced works from other authors Takagi et al. (2007, 2003); Shimizu et al. (2007) and Lee et al. (2005). The model parameters such as drag and added mass coefficients and the spring rate of the interconnections are modeled after the values provided in Takagi et al. (2003). Figure 3.9 shows a scheme of the knots and bars modeling, both elements are represented as point masses with different hydrodynamic parameters, resumed in Table 3.3.

The equations of motion for the fishnet and the freely moving objects representing the load, are formulated in this work under the framework of the DEM. The point masses that shape the net are placed at each knot and at the center of the mesh bars connecting each pair of knots.

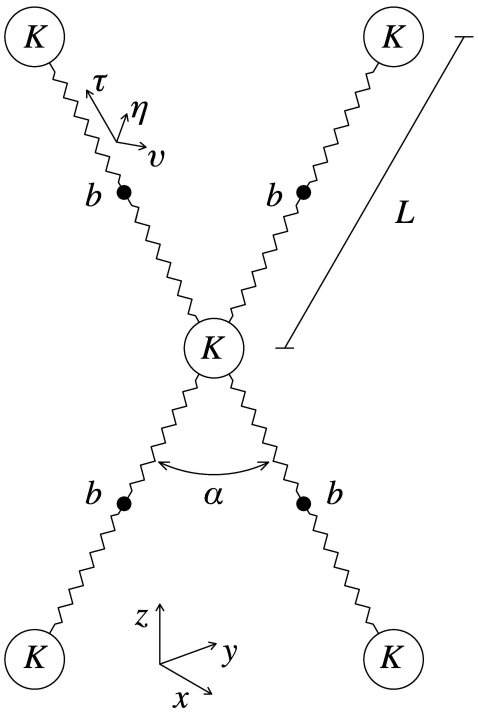

Figure 3.9: Domain for the Fish Net Tunnel simulation.

Table 3.3: Hydrodynamic coefficients of bars and knots

	Knots	Bars		
		τ	η	ν
C_D	1.0	0.1	1.2	1.2
C_L	0.5	0.0	1.0	1.0

For the example presented here, the fishnet is made up from 1550 knots disposed in 50 concentric circles of 31 knots, and the corresponding 3100 bars. Freely moving objects are also added representing the load, modeled as a set of 90 uniform radius spheres.

Each element of the system, except for the freely moving objects, is subject to internal forces derived from the elasticity of the mesh bars and the location of the knots. Also external forces are applied to each object, including weight, buoyancy, drag and induced mass. The contact between the freely moving objects and the knots and bars of the fishnet might also generate additional forces on the corresponding elements.

Each knot point is assumed to be a spherical object, so the drag and induced

mass coefficients are assumed to be the equal in every direction of motion. Their values are given in the first column of Table 3.3. The equation of motion for each knot i is given in Eq. (3.60), where $\vec{a}_i$ is the acceleration vector for the knot, M_i its mass, Vol_i its volume, ρ is the fluid density, and the vectors $\vec{T}_i$, $\vec{W}_i$, $\vec{B}_i$, $\vec{D}_i$, $\vec{F}_i$, are respectively the elastic tension, weight, buoyancy, drag force and interaction with fishing load force.

$$\vec{a}_i \cdot (M_i + \rho \cdot Vol_i \cdot C_{Mi}) = \vec{T}_i + \vec{W}_i + \vec{B}_i + \vec{D}_i + \vec{F}_i \tag{3.60}$$

On the other hand, the mesh bars are modeled as cylindrical elements and the fluid forces vary with different flow directions of relative fluid velocity, thus it is needed to transform the forces applied to each bar into the local system of the corresponding bar, add them together and the transform back again to the global reference system. Both coordinate systems are shown in Fig. 3.9. The equation of motion of the i bar is completed in three steps, Eq. (3.61), Eq. (3.62) and Eq. (3.63)), where TM_i is the transformation matrix between the reference coordinate system and the i bar local coordinates, and the supra index $'$ represents that the vector is expressed in the local, body-fixed coordinates of the bar. The first step calculates an intermediate acceleration, $\vec{a'}^*_i$, that sums the terms of elastic tension, weight, buoyancy and drag, note that the elastic tension and drag forces are calculated directly in the local coordinates. In the second step the intermediate acceleration in the bar local, body-fixed coordinates, is transform to the global coordinates, and in the last step the contact force due to the load is added directly in the global coordinates.

$$\begin{aligned}
\vec{a'}^*_i \cdot (M_i + \rho \cdot Vol_i \cdot C_{Mi}) &= \vec{T'}_i + \vec{W}_i \cdot TM_i + \vec{B}_i \cdot TM_i + \vec{D'}_i && (3.61)\\
\vec{a}^*_i &= TM_i \cdot (\vec{a'}^*_i)^T && (3.62)\\
\vec{a}_i &= \vec{a}^*_i + \vec{F}_i && (3.63)
\end{aligned}$$

Finally, for the freely moving objects representing the fishing load, the elastic forces are dropped and full fluid force DC_i is computed directly from the fluid solver due to the larger size of this objects, by means of the immersed boundary method. Equation (3.64) hold for these objects.

$$\vec{a}_i \cdot M_i = \vec{W}_i + \vec{B}_i + \vec{DC}_i + \vec{F}_i \tag{3.64}$$

These equations have the position and velocity of each knot point and mesh bar implicit in the tension and drag force, so the displacement of the device is given by a system of ordinary differential equations. The equations can be solved numerically for each point, given an initial position of the net. Shimizu et al. (2007) introduces a Fishing Net Shape Simulator (NaLA) that incorporates the sixth order Runge-Kutta method for solving the ordinary differential equation system to simulate a bottom gill net. It was found that the fourth order Runge-Kutta method Ferziger and Peric (2002) gives the best performance to solve the ordinary differential equations system, in this case. Equations (3.65) summarize the method where ϕ is the vector with the velocity and position of every element of the system and f is the vector containing the acceleration and velocity calculated with and the corresponding time.

$$\phi^*_{n+\frac{1}{2}} = \phi^n + \frac{\Delta t}{2} \cdot f(t_n, \phi^n) \tag{3.65a}$$

$$\phi^{**}_{n+\frac{1}{2}} = \phi^n + \frac{\Delta t}{2} \cdot f(t_{n+\frac{1}{2}}, \phi^*_{n+\frac{1}{2}}) \tag{3.65b}$$

$$\phi^*_{n+1} = \phi^n + \Delta t \cdot f(t_{n+\frac{1}{2}}, \phi^{**}_{n+\frac{1}{2}}) \tag{3.65c}$$

$$\phi^{n+1} = \phi^n + \frac{\Delta t}{6} \cdot \Big[f(t_n, \phi^n) + 2f(t_{n+\frac{1}{2}}, \phi^*_{n+\frac{1}{2}}) + 2f(t_{n+\frac{1}{2}}, \phi^{**}_{n+\frac{1}{2}}) + f(t_{n+1}, \phi^*_{n+1}) \Big] \tag{3.65d}$$

The time step required for solving the fishnet equations might not be the same required by the flow solver for the given flow conditions. In the simulations presented in this work, for every time step of the fluid solver the Runge-Kutta is executed 100 times to reach the convergence of the system.

To obtain the external forces acting on the fishnet, the fluid flow properties at each time step and the location of each element of the fishnet are required in order to compute the drag forces. The velocity is obtained by a search and interpolation routine that interrogates the finite volume grid for each lumped mass location. The drag forces are then calculated and applied to both the fishnet and the fluid. The forces on the fishnet are incorporated at each lumped mass, while the force applied to the fluid is first filtered with a Gaussian distribution back into the finite volume grid in the fluid cells nearby each element of the fishnet and then added in the source term. This procedure is iterated within each time step until a specified convergence criteria.

Chapter 4

Results

This chapter describes the results of the numerical methods for modeling both the vorticity wind turbine (VWT) and the fish net tunnel, including the validation for the latter by comparing it with results from a physical test in a towing tank. Several variables are considered for the analysis of the VWT simulations, including displacement, velocity and prediction of output power. The chapter will also include an interpretation of the behavior of the fluid flow around the bodies.

4.1 Fish net tunnel

A physical towing tank test was carried out to compare the simulated with an experimental case. Figure 4.1 shows the configuration adopted by the net at four different time steps during the simulation and Fig. 4.2 the shape adopted during the experimental test in the same conditions. In the upper panel of Fig. 4.1 (panel *a*) the initial configuration of the net has the conic shape described in the previous section and the load is disposed at the entrance of the net represented as a set of free balls. As time advances, the load starts to be dragged by the flow and interacts with itself and the net. Subject to the drag of the fluid and the interactions with the load, the net adopts a bulb shape at the downstream end and a constriction in the middle.

The form adopted by the fishnet in the numerical simulation compares qualitatively well with the one observed at the towing tank test. In the simulation the load tends to expand further, this may be due to several reasons, the two main ones being the elasticity of the bars and the shape of the objects

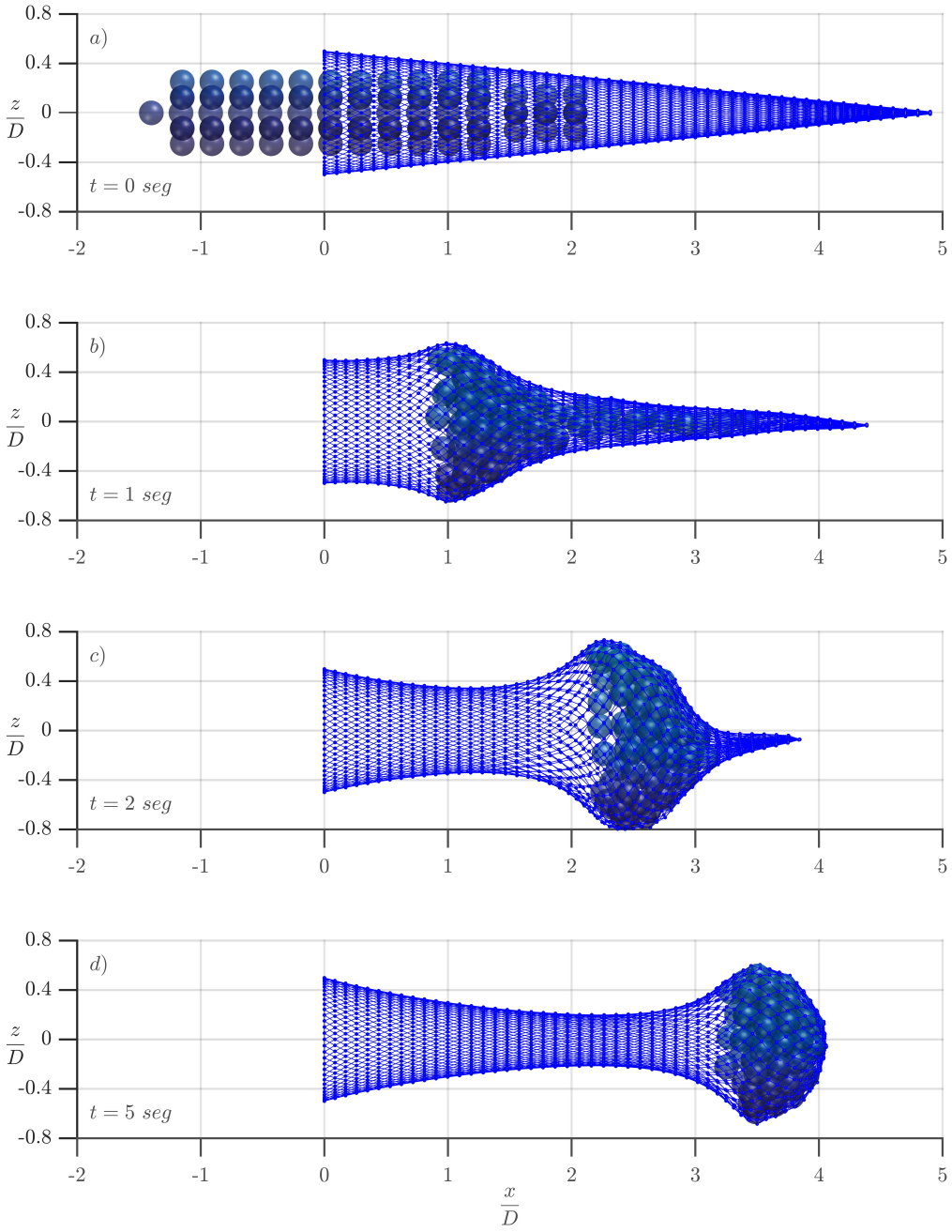

Figure 4.1: Evolution of the fishnet shape during the simulation as the load is dragged into the fishnet at four time steps; a) $t = 0\,s$, b) $t = 1.0\,s$, c) $t = 2.0\,s$ and d) $t = 5.0\,s$.

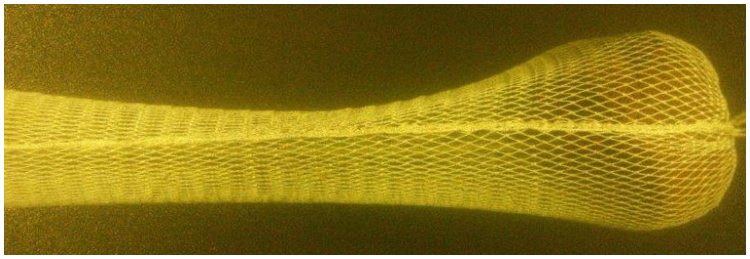

Figure 4.2: Shape of the Fish Net during towing tank test.

representing the load. The bars in the numerical model might be given a lower elastic constant than those in the experimental fishnet. Also the load used in the experimental test were plastic bottle caps while in the simulation larger uniform radius spheres were used. These spheres produce a greater blocking on the fluid flow, giving place to significant radial components on the flow velocity. Figure 4.3 shows the stream lines of the fluid flow. The green lines are the stream lines that are far from the load of the fishnet and red lines are the stream lines that cross the bulb in between the load spheres. It can be seen that the red stream lines acquire radial components in the bulb zone, eliciting the large dispersion of the load, and chaotic behavior with recirculation immediately after the bulb.

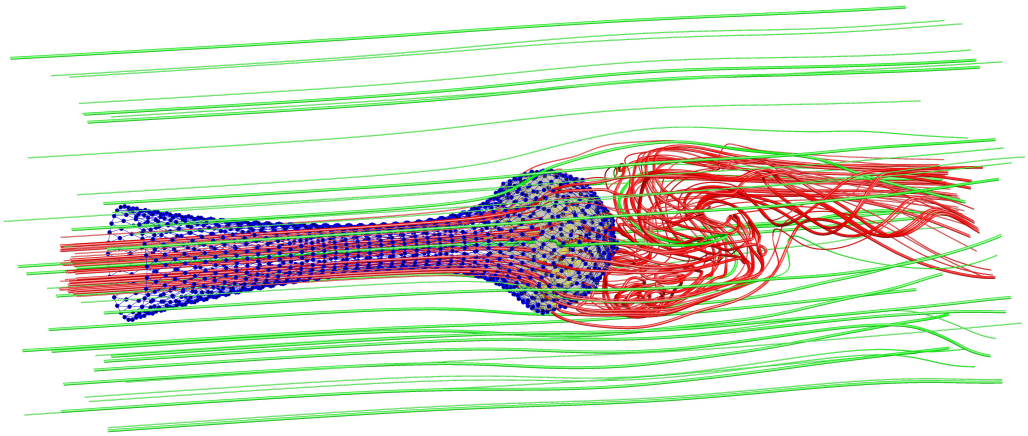

Figure 4.3: Stream Lines around the Fish Net; the red stream lines cross the bulb in between the spheres; the green stream lines are far from the load

The simulation model represents the motion of the elements by hydrodynamic interaction with the fluid. This interaction is bidirectional, this mean that the flow affects the system elements and vice versa. To this end, once calculated the force on the element an equal and opposite force is applied on

the fluid, previously filtered with a Gaussian distribution, in the neighboring cells where the item is located. In Figure 4.4 the velocity profile is plotted at three different places as indicated in Fig. 4.5 with letters A, B and C. Each graph a, b and c, contains three plots, the dotted lines are the profile that the flow adopt just before the fish net (letter A in Fig. 4.5), the continuous line is the velocity profile at the bulb (B) and the slash-dotted line the profile

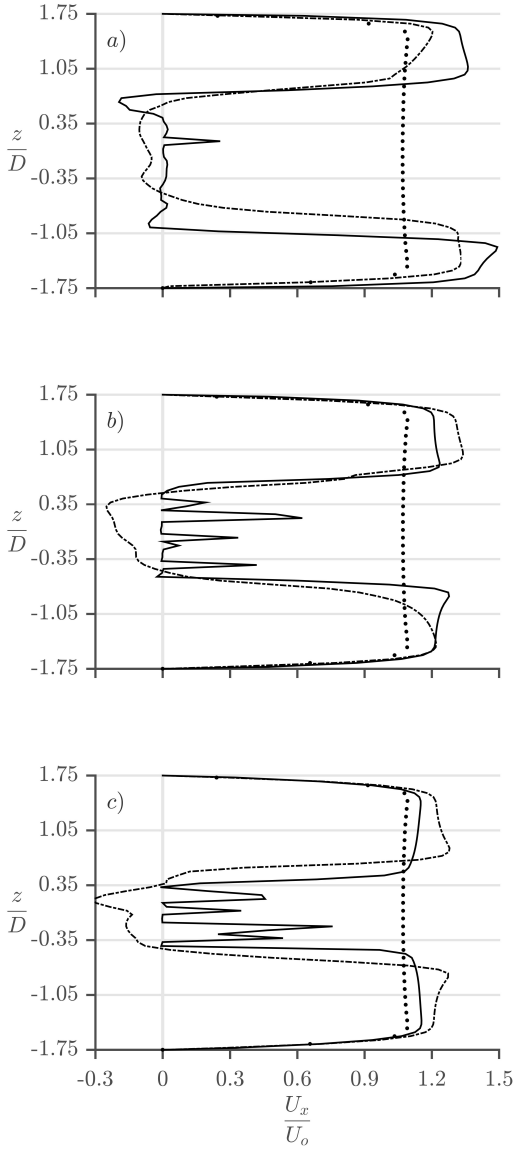

Figure 4.4: Velocity profiles at different cross sections along the fishnet, and for three values of Ψ. Graph *a*) is for $\Psi = 1$, *b*) for $\Psi = 0.8$ and *c*) for $\Psi = 0.6$. The dotted line is the velocity profile at A, the continuous line at B and the slash-dotted line at C

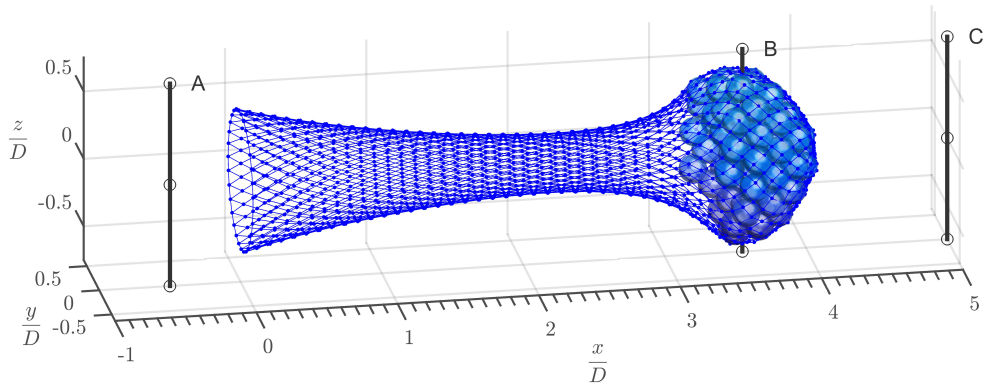

Figure 4.5: Three dimensional view of the shape adopted by the Net in the simulation and indication of the position of the velocity profiles plotted.

after the fish net (C), where recirculation occurs. In order to represent the free bodies of the load as independent bodies with the immersed boundary method IBM it is necessary to define the object radius of the IBM smaller than the real object radius. Because of this the tuning parameter Ψ of the model is defined in Eq. (4.1) as the quotient of the IBM radius (R_{Ximb}) and the object real radius (R_{obj}).

$$\Psi = \frac{R_{Ximb}}{R_{obj}} \tag{4.1}$$

In Figure 4.4 the three different axis (a, b and c) plot the velocity profile at the three positions of Fig. 4.5 for $\Psi = 1$ in panel a, $\Psi = 0.8$ in panel b and $\Psi = 0.6$ in panel c. As it can be seen in Fig. 4.4 smaller values of Ψ generates more transversal flow through the bulb (continuous line) while greater values tend to represent the load as one big peace of load generating complete blocking of the flow. In this work all the results are presented for $\Psi = 0.8$, anyway further experiments are needed to determine a right value of transversal flow through the bulb.

The mesh angle α (see Fig. 3.9) is a very important design property; the selectivity of the fish net depends on this, a much closed mesh would not allow baby fishes to scape and preserve the species. In Figure 4.6 the grey dots indicate the mesh angle α and the continuous line represents the mean by section within the x direction. Further experiments are currently being organized to obtain mesh angel measurements from the experimental campaigns in order to compare those to the numerical results.

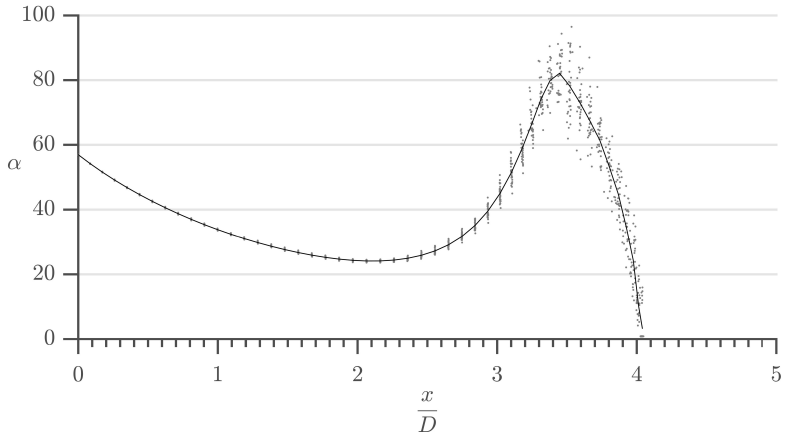

Figure 4.6: Mesh angle of the fish net.

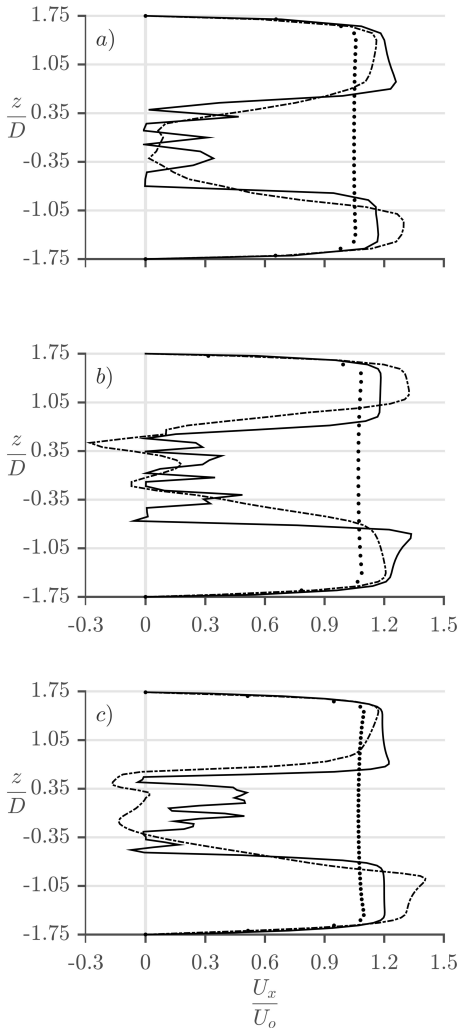

Figure 4.7: Mesh independence study. Velocity profiles for three sizes of mesh, *a)* $\Delta\, l_a = 2 \cdot \Delta\, l$, *b)* $\Delta\, l_b = 1.25 \cdot \Delta\, l$ and *c)* $\Delta\, l_c = 0.75 \cdot \Delta\, l$

To study the mesh independence several simulations were carried on. In this work all the results are presented for the Cartesian grid described in Section 3.3, with cubic control volumes of size $\Delta\, l = 1\, cm$. In Figure 4.7 the velocity profile adopted by the flow, in the same three planes as indicated in Fig. 4.5, are presented. The tuning parameter used in this simulations is set to $\Psi = 0.8$, so these profiles should be compared with Figure 4.4b. In the graphs of Fig. 4.7, the coarser mesh corresponds to plot a with eight times less control volumes, $\Delta\, l_a = 2 \cdot \Delta\, l$, in plot b $\Delta\, l_b = 1.25 \cdot \Delta\, l$ and in plot c the number of control volumes is around the double with $\Delta\, l_c = 0.75 \cdot \Delta\, l$.

As the grid gets smaller, this is better definition, the IBM module can represent better the spherical shape of the elements of the load and so the free spaces between the spheres. While some details of the flow across the bulb seem to be smeared out for the coarser resolution, the results remain qualitatively comparable, specially for the three finer resolutions, suggesting that the flow is sufficiently resolved for these conditions.

Finally the influence of blending coefficient between upwind and centered discretization for the convective terms in the flow solver, as well as of turbulence modeling, is shown in Fig. 4.8, depicting velocity field magnitude at a horizontal mid-plane for two simulations. Results from a simulations with blending coefficient 0.7 and no turbulence model are given in the upper panel, while results from a simulation with blending coefficient 0.95 and a simple large eddy simulation (LES) Smagorinsky turbulence closure are given in the lower panel. Velocity fields from both simulations seem rather similar to each other, although in the simulation with a lower blending coefficient wake structures seem to be smeared as expected.

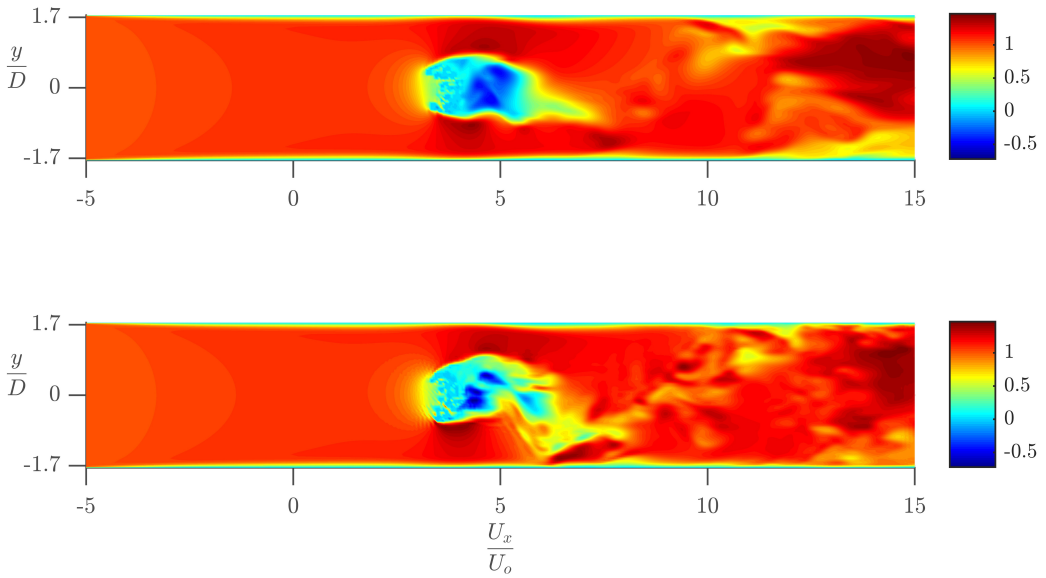

Figure 4.8: Comparison of velocity field of two simulations, the upper panel does not represent turbulence, bottom panel has turbulence modeling activated with bending coefficient 0.95

4.2 Vorticity wind turbine

The modeling of a vorticity wind turbine (VWT), as explained in the previous chapter, was carried through and simulated numerically with caffa3d.MBRi. Results are presented in this section, in a first instance, for a uniform air flow of $U_o = 9.1 \cdot m/s$, as this is the critical velocity found in the structural analysis Section 3.1, the Reynolds number calculated at the equivalent height z_e= $8.4\,m$ (where the radius is D_{ref} = $0.77\,m$) for the critical velocity is $Re = 4.67\,E5$. Following that, a sensitivity analysis to wind speed and other relevant parameters will be shown.

Figure 4.9 shows the dimensionless transversal displacement of the top of the rod, where the magnet is located, for a 30 second simulation with uniform air flow of $U_o = 9.1\,m/s$. The oscillatory response shows that the lock-in effect is well captured by the coupled simulation, and that the device is taking energy from the fluid. This is evidenced by the sinusoidal displacement, of amplitude $A = 0.2\,D_{ref}$, which correlates with the graph of the transversal displacement for structures under the lock-in effect from Section 2.1. The response shows different frequencies, distinguishable from the slight difference between peaks and valleys presented in the figure, anyway the main oscillatory frequency of the turbine can be calculated from Fig. 4.9, f= $1.26\,Hz$.

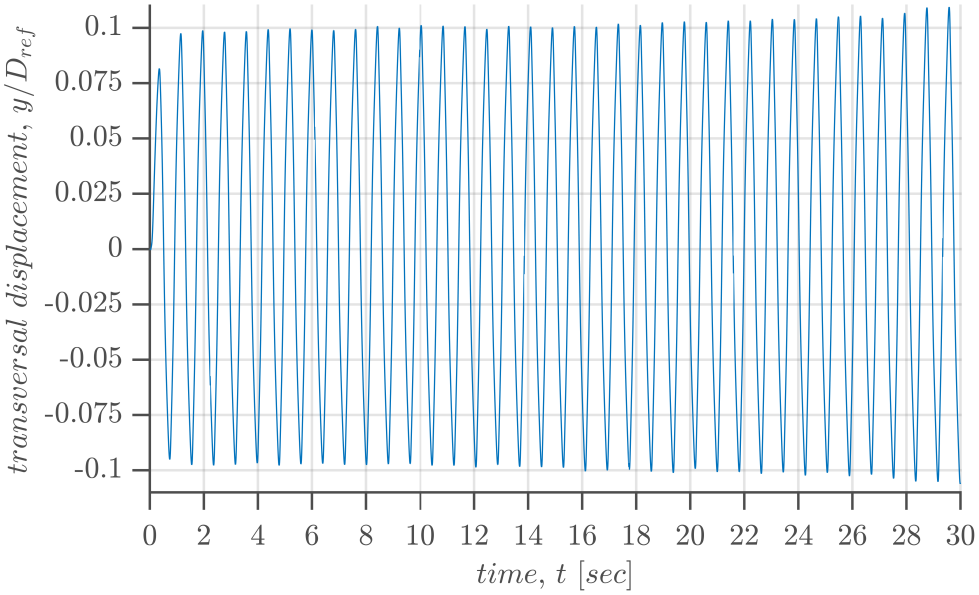

Figure 4.9: Dimensionless transversal displacement of the top of the rod, where the magnet is located.

Note that at the top of the mast, the amplitude of the oscillations are much wider. For the same simulation, the amplitude of the transversal displacement at the top of the mast is twice its diameter, which is quite bigger than the one predicted in Section 3.1. This is illustrated in Fig. 4.10 for an interval of five seconds of the simulation. It can also be seen the sinusoidal response with greater detail.

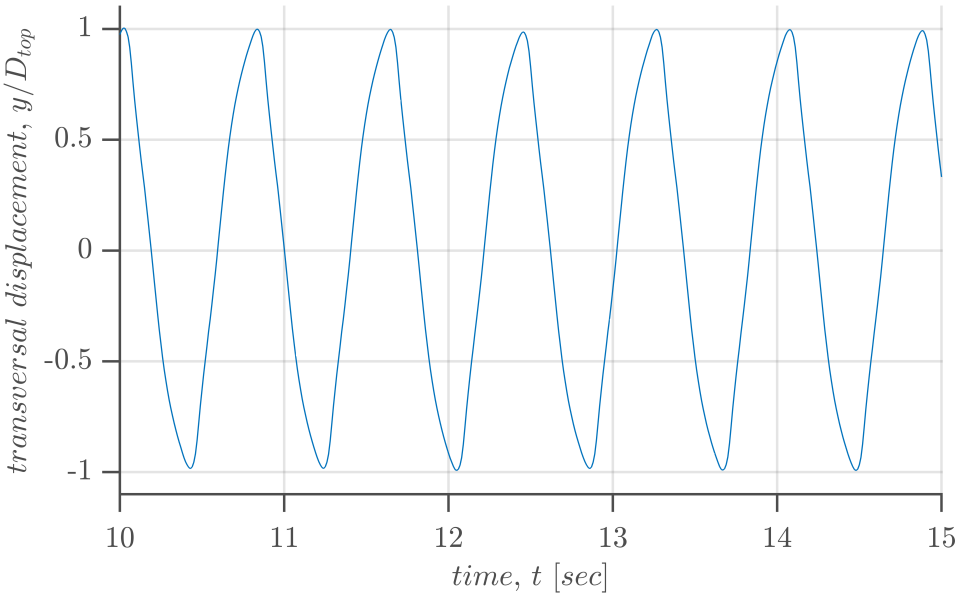

Figure 4.10: Dimensionless transversal displacement of the top of the mast for a five seconds interval of the same simulation

In order to be able to determine the frequency of the vortex shedding, the in-plane vorticity, ω_k, defined in Eq. (4.2), is calculated in three monitoring points at every 0.01 seconds and plotted vs time in the upper panel of Fig. 4.11. The three monitoring points are set for the same x and y coordinate components, downstream the turbine, and at three different heights, z_1, z_2 and z_3 (corresponding to 20%, 50% and 80% of the height of the mast respectively). In the discretized domain, the two-dimensional vorticity is calculated with the least-square method in Eq. (4.3).

$$\omega_k = (\nabla \wedge \vec{v}) \cdot \hat{k} \tag{4.2}$$

$$Vor = -\frac{2 \cdot v_{i+2,j} + v_{i+1,j} - v_{i-1,j} - 2 \cdot v_{i-2,j}}{10 \cdot \Delta x} + \frac{2 \cdot u_{i,j+2} + u_{i,j+1} - u_{i,j-1} - 2 \cdot u_{i,j-2}}{10 \cdot \Delta y} \tag{4.3}$$

Where i is the cell index of the $x-coordinate$ and j the cell index of the $y-coordinate$, u is the velocity component in $x-direction$ and v in $y-direction$, and Δx and Δy are the distance between two consecutive computing points in x and $y-direction$ respectively.

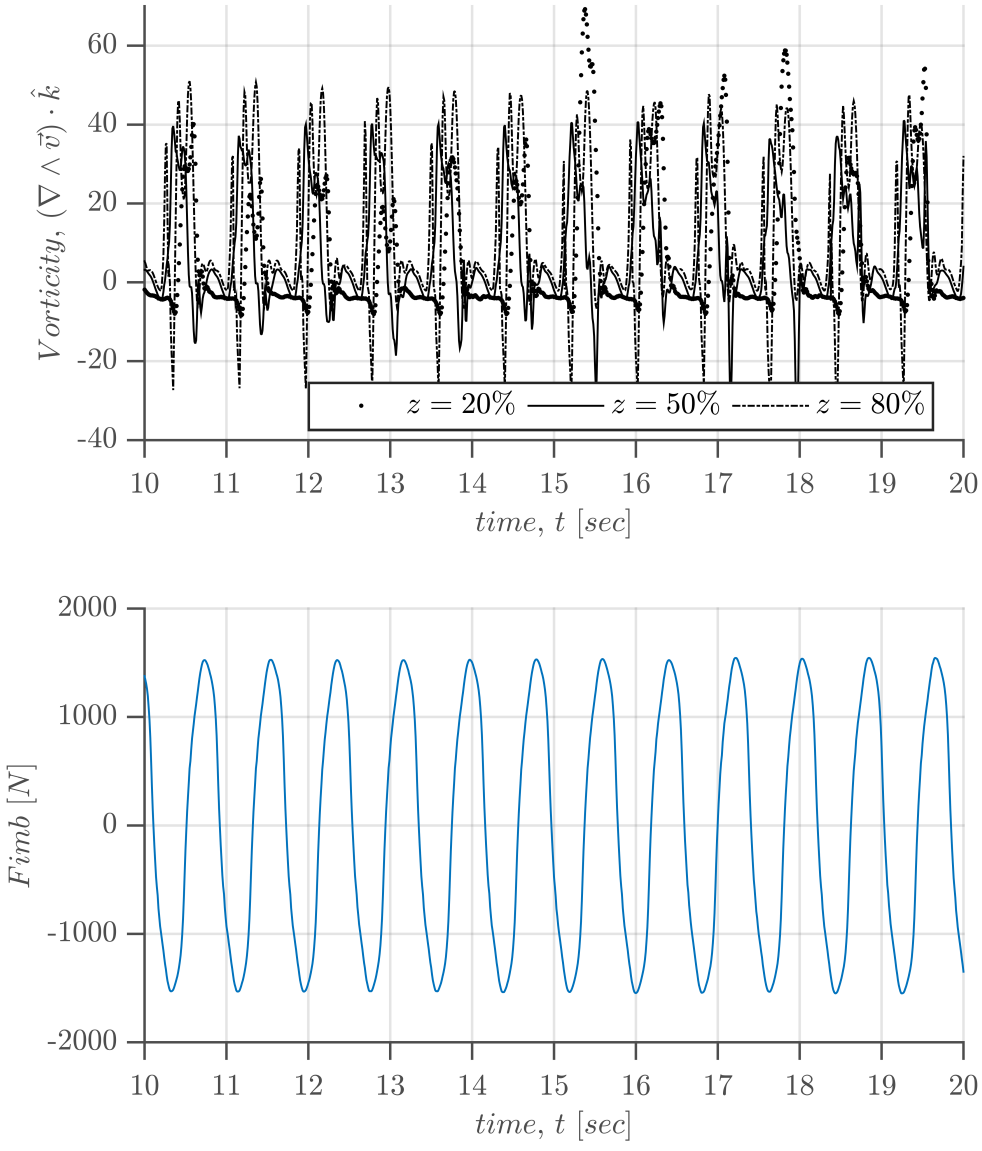

Figure 4.11: In-plane Vorticity calculated at three monitoring points corresponding to 20, 50 and 80 % of the length of the mast (upper panel) and transversal force vs time (bottom panel)

Two important concepts are drawn from the plotted data in the upper

panel of Fig. 4.11. First of all, the frequency of the vortex shedding can be determined, f_{vs}= $1.25 \cdot Hz$, and secondly it can be seen that the shedding is synchronized along the height of the mast. Because of this, the transversal force integrated along the structure, at a given instant of time, will be maximized. Otherwise, opposing forces will coexist along the structure, and the resulting force will be reduced. The bottom panel plots the integrated transversal force acting over the mast. Here the frequency of the force can be obtained and compared with the vortex shedding frequency, which turn out to be the same, as expected.

The vorticity can also be calculated for all the computing points of a $x-y$ plane and plotted as a vorticity field. This is presented in Fig. 4.12 for $z = z_{eq}$ at two instants of time. The black triangle inserted over the field represents the monitoring points used in Fig. 4.11. All three points occupy the same exact point in the field, as it is a top view of the turbine. It can be seen in the figures that at the specific instant of time of Fig. 4.12a the vortex is getting detached from the left side of the mast (in the range of positive values of the $y-$coordinate), with negative value of the vorticity (ω_k). While in Fig. 4.12b (0.41 seconds later) the vortex is getting detached from the right side (in the range of negative values of the $y-$coordinate), with positive values of vorticity. This denotes how the vortex are alternatively detached from one side and

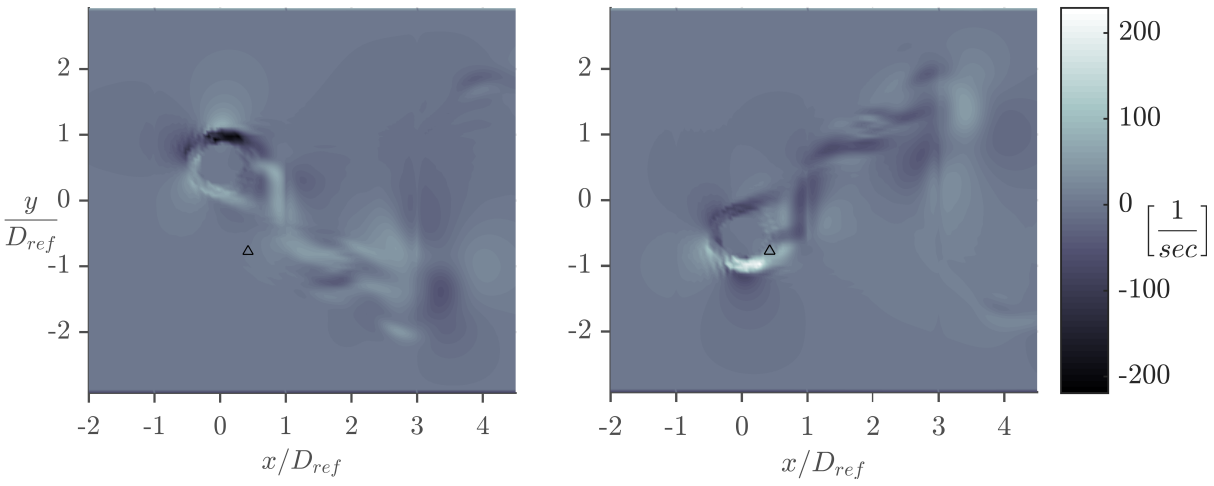

(a) Vorticity field at t=14.90 seconds of simulations

(b) Vorticity field at t=15.31 seconds of simulations

Figure 4.12: Upper view of the in-plane vorticity field at a height of $z = z_{eq}$.

another of the mast, and that the local spinning of the fluid runs in opposite rotation directions at each side and another of the turbine.

Figure 4.13 shows a three dimensional view of the simulation with the respective streamlines of the flow around the volume. The red streamlines are closer to the mast and display chaotic behavior downstream, while the green streamlines are further away and then only a slight deviation is observed. In the figure is also observed that at the top of the mast, the streamlines flow over the obstacle.

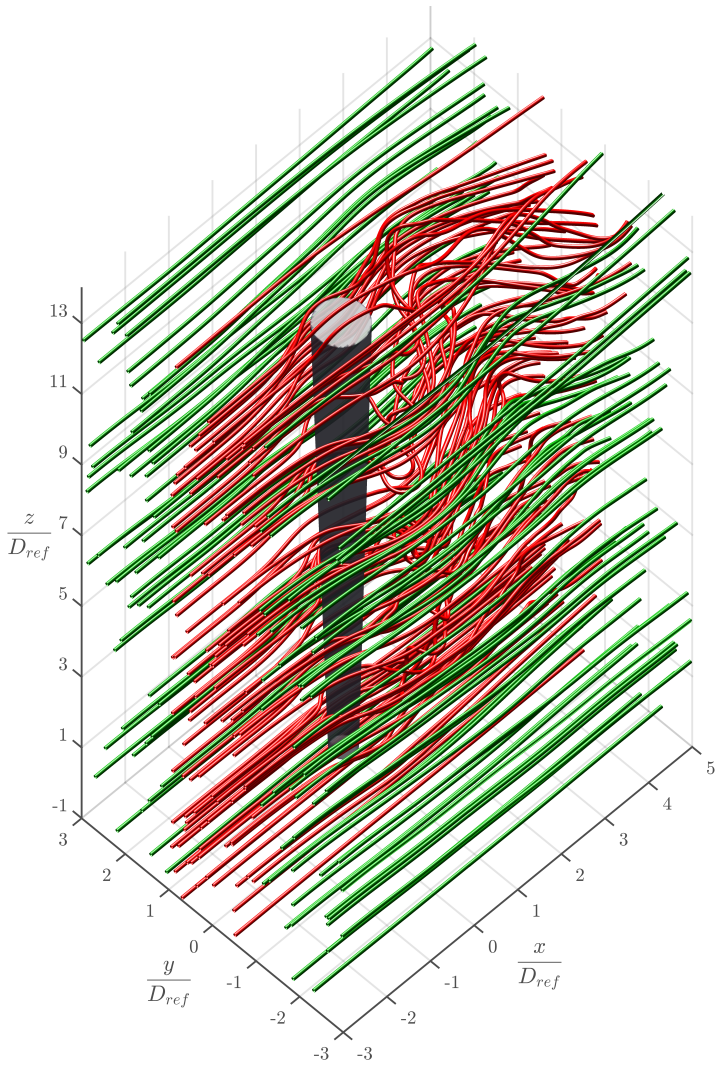

Figure 4.13: Three dimensional view of the vorticity wind turbine with streamlines. The red streamlines are close to the mast and shows chaotic behavior downstream, while the green streamlines are further away and only a slight deviation is observed.

To quantitatively assess the output energy production, the calculations of Section 3.2.3 were followed. In Figure 4.14 three plots are shown: the upper panel plots the velocity of the last element of the rod (where the magnet is fixed, and thus this velocity is equal to the magnet velocity) during the 10 seconds of the simulation. The mid panel plots the magnetic force calculated at every time step for a generator with the properties of Table 3.2 connected to a resistive load of $R = 7\,\Omega$. Multiplying these two values (magnet velocity and magnetic force) at every time step, the instant output electrical power is obtained, plotted in the bottom panel together with the instant mechanical power available in the last element of the rod, the latter calculated as expressed in Eq. (4.4).

$$P_{mec} = M_{imb,x} \cdot \omega_x + F_{imb,y} \cdot v_y \tag{4.4}$$

If the instantaneous output electrical power is divided by the power available in the fluid flow (constant in time for a uniform flow), the instantaneous efficiency of the system is obtained.

$$\overline{P}_{wind} = 1/2\,\rho\,U^3\,A_{VWT} \tag{4.5}$$

Here A_{VWT} is the transversal area of the VWT, The same calculations can be done considering the swept area (A_{sw}), this is the total area covered by the oscillations, as proposed by Barrero-Gil et al. (2012). With this approach smaller values of efficiency are reached, which turn to be more convincing.

$$\eta^* = \frac{P_e}{1/2\,\rho\,U^3\,A_{sw}} \tag{4.6}$$

This is plotted in Fig. 4.15 for the last five seconds of same simulation, here a peak efficiency of $\eta_{peak} = 0.223$ is reached, and integrating during the period of the simulation and dividing by the time lapse, an integrated efficiency of $\overline{\eta^*} = 0.0944$ is reached. For a discretized in time system the integrated efficiency is calculated as:

$$\overline{\eta^*} = \frac{1}{N_{steps} * \Delta t} \sum_{1}^{N_{steps}} \eta^* \cdot \Delta t \tag{4.7}$$

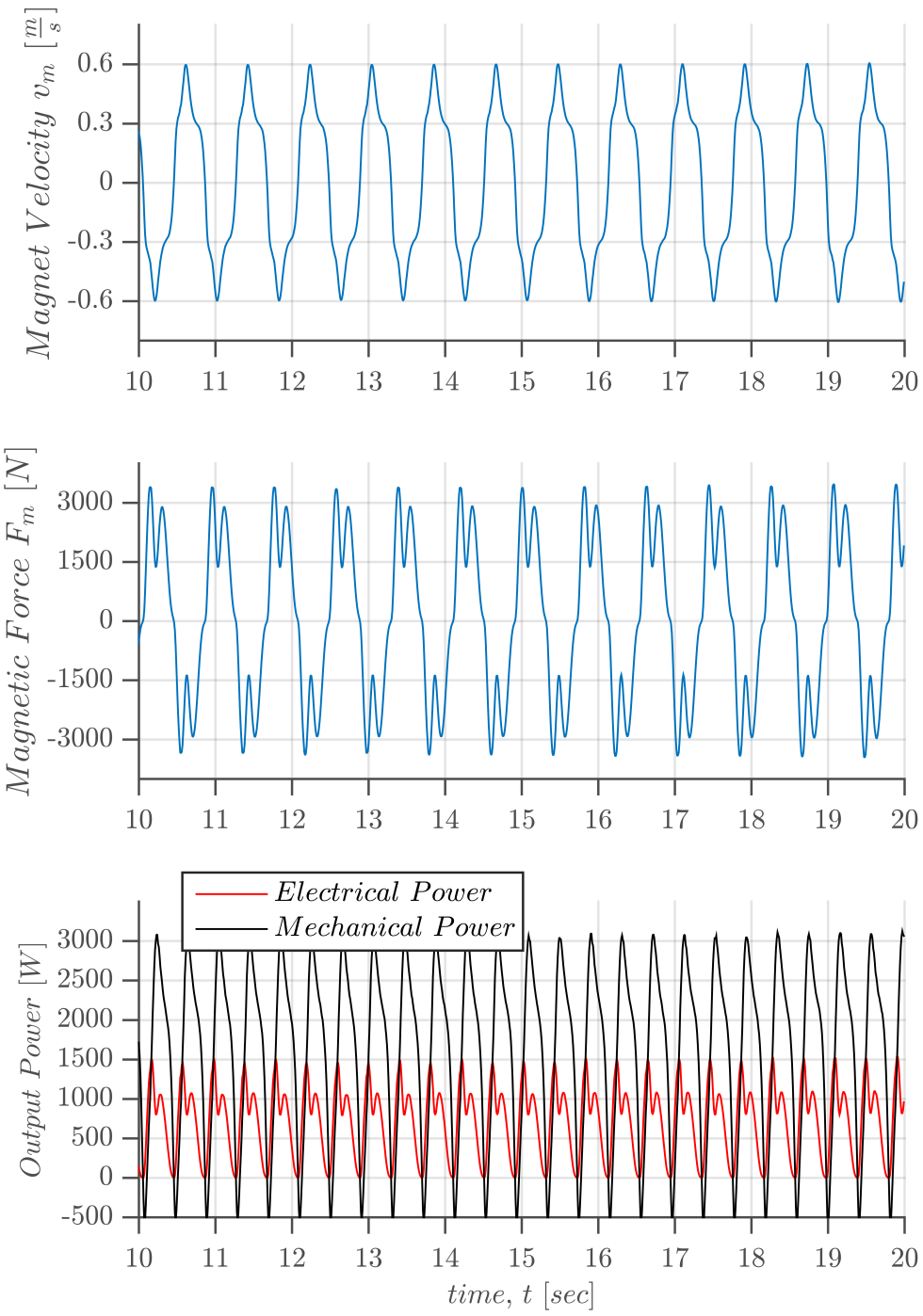

Figure 4.14: Plot of the magnet velocity (upper panel), magnetic force (mid panel), and instantaneous mechanical and electrical output power (bottom panel), during 10 seconds of simulation with uniform wind velocity of $v_{wind} = 9.1\, m/s$.

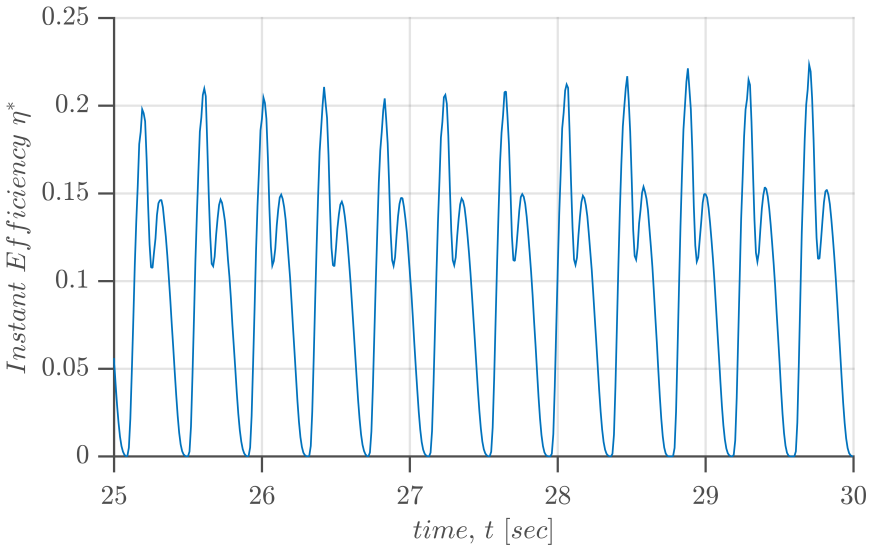

Figure 4.15: Instantaneous efficiency

The magnetic force presents a relatively small valley in the peak of the main sinusoidal component of the magnetic force and vice-versa (see mid panel of Fig. 4.14), this is then transmitted to the output electrical power (bottom panel), and to the instantaneous efficiency Fig. 4.15. These smaller valleys presented in the main peaks can be explained by analyzing the relative displacement of the magnet from one coil to the other. In Figure 4.16 the magnet transversal displacement and the magnetic force are plotted together in left and right vertical axes respectively for two cycles of the oscillation of the VWT. In the figure the two coils are also represented by the grey lines, the continuous ones correspond to the center of each coil and the dashed ones represent the ends.

Defining two zones in the displacement of the magnet, zone I when the blue line (magnet location) is in between the two coils (white area), and zone II when it is in the shaded area, note that at every cycle each zone is crossed twice. When the magnet is located in zone II, it means that it is inside a coil, and as the magnet is represented punctually, the induced currents in the coil at one side and another of the magnet will be opposed, causing a reduction of the magnetic force and thus of the output power. Anyway, zone II is a zone of low velocity, as it even reaches zero at the peak of the displacement, where the magnetic force became null, and so the reduction of the magnetic force is not critical. When the magnet is in zone I, it is located between the two coils, and here the distance from the magnet to each coil plays an important role in

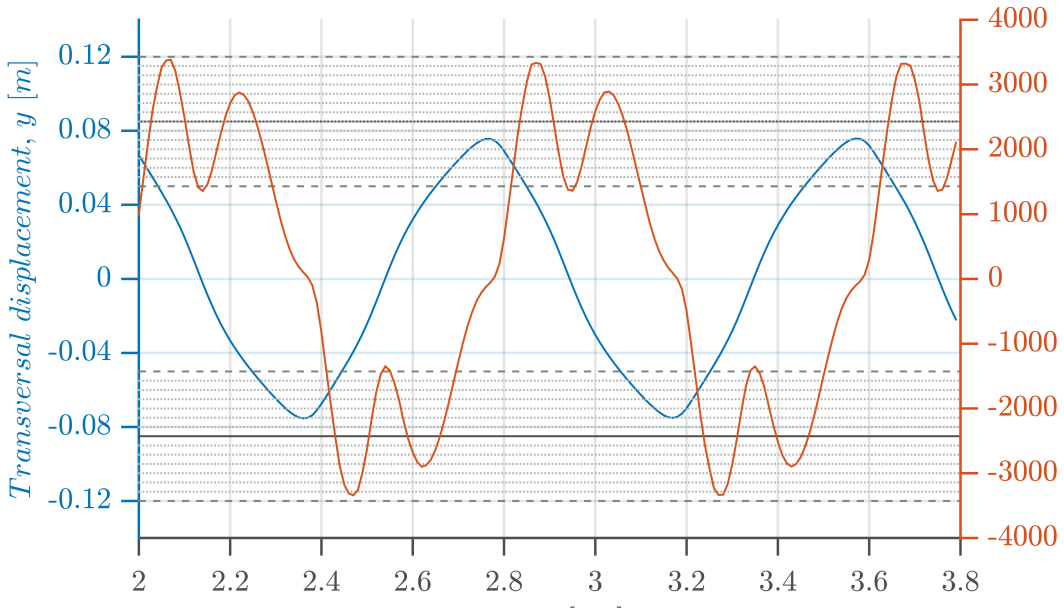

Figure 4.16: Plot of the magnet transversal displacement (left blue axis) and the magnetic force (right red axis). The position of the center of the coils are illustrated by the grey continuous lines and the borders of the coils by the grey dashed lines. Simulation with uniform wind velocity of $v_{wind} = 9.1\,m/s$.

the magnitude of the force. Note that a maximum peak is presented when the magnet is next to a coil end. This is because no opposite currents coexist in the coil, and the distance to the coil is the minimum. As the magnet moves away from one coil is getting closer to the other, this means that the magnetic force exerted by the first coil start to decrease while the other increases. But as the coils are relatively far, when the magnet is in the middle between the two coils there is a small valley besides the velocity is maximum.

The results shown so far, correspond to the same simulation, having a uniform flow velocity of $U_o = 9.1\,m/s$, and two equal resistive loads of $R = 7\,\Omega$ connected at each coil of the generator model. Several simulations where carried out varying alternatively the wind velocity and the resistive load. For each simulation the integrated efficiency was calculated and plotted in Fig. 4.17 against the wind velocity. The different colors indicate different values of load resistance connected to the coils.

The curves presented in Fig. 4.17 are generally continuous, displaying growing behavior. As the efficiency at low values of wind speed is almost zero, it improves the values for mid wind velocities (shown the horizontal axis), and significantly higher values are reached for higher wind speeds. This is mainly

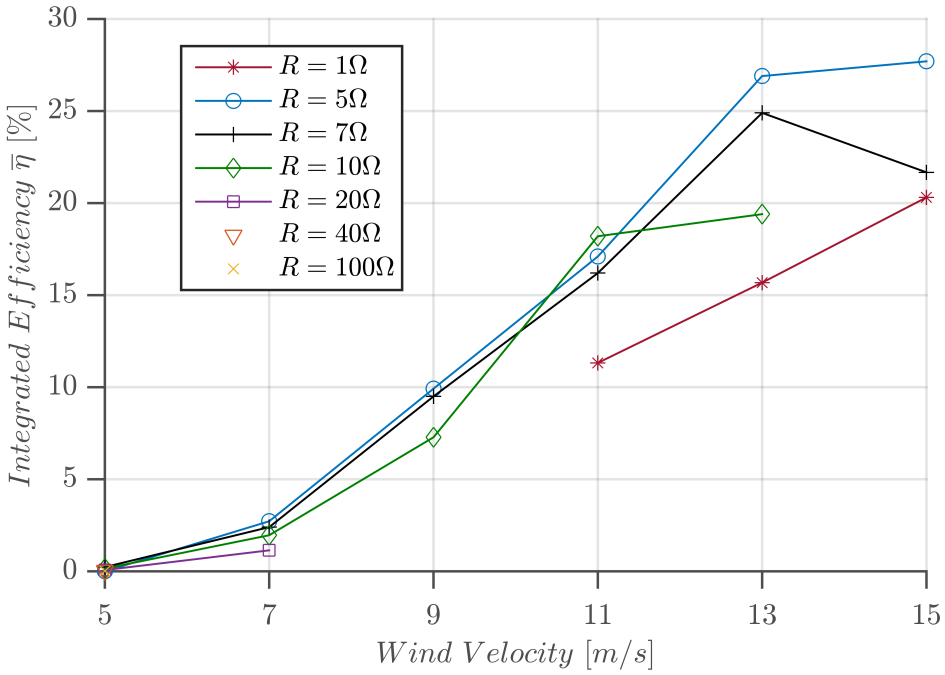

Figure 4.17: Efficiency vs wind speed parametric in load resistance

for the structural damping of the rod. For low values of wind velocity, low forces are applied, and so the energy disipated in the material is enough to keep the oscillations within a range of very small amplitude. On the other hand, for high valuess of wind speed the rod adopts large deformations and the amplitude of the oscillations become much wider, reaching higher velocities and forces, hence generating higher values of power. This large deflections on the rod may not be really convenient, as it it may make it prone to malfunction or even risk breaking it, but as the model does not actually implement fracture prediction, it returns high values of output power instead.

4.2.1 Limitations

The results presented in the previous section describe a VWT adjusted to operate at a wind speed of $v_{wind} = 9.1\, m/s$, seeking to maximize the output power, and thus, the efficiency of the device. However, it was found that at different wind speeds, the same turbine would operate with lower values of efficiency. Also some chaotic behavior of the structure was found at much higher values of wind speed, as the forces that the wind exerts over the structure are so significant. This chaos could follow several patterns:

- The frequencies of oscillations are much higher than the frequency of the vortex shedding tabulated for the corresponding Reynolds number.
- The amplitude of the oscillations obtained turned out to be disproportionately big.
- The output power is higher than the power available in the fluid.
- The mechanical power in the rod is higher than the available in the fluid (both are results that actually contradict the laws of thermodynamics).

This phenomenon may be explained because the time step used is not small enough to capture the motion of the mast, hence several cells are crossed by the mast in only one time step, causing erratic and unmeasurable forces over the mast that, when transmitted to the rod, create the illusion of physically unfeasible phenomena. Some testes were carried on, using shorter time steps, but so far the exact combination of time steps (Δt_{dem} and dt) has not been found yet, as it would vary for different values of wind speed.

Anyway, these irregularities could be avoided testing a more damped structure, as it would support larger forces. This can be achieved by changing the entire rod, for instance using a thicker one or changing the properties of the material (i.e using one with higher structural damping), but this is not a functional option, as it would not be actually possible in a real physical setting to change the rod in order to accommodate the system for different wind speeds. A solution that would be both physically feasible and logistically sound would be to implement a variable damping system.

As the model of the generator implemented in these simulations can be interpreted as a damping force in the motion of the rod, by varying the parameters of the generator, the damping of the structure could be measurably modulated. The key is to find a set of parameters for the generator that can

maintain the amplitude and velocity of the oscillations within a controlled range while at the same time maximizing the output power. In this case, the resistive load connected to the circuit of the generator would be used to tune the damping, so as to analyze the behavior at different time steps. Eq. (3.54) and Eq. (3.55) explain the inversely proportional relation between the magnetic force (damping) and the value of the load resistance. There is available technology that could, after measuring the wind speed, automate the adjustment of the damping to optimize the power generation under each specific wind conditions.

Chapter 5

Conclusions and Future work

The main objective of the present research was to understand, through the use of mathematical models, the potential efficiency of a vorticity wind turbine. In the process of devising the tools to achieve that goal, a three-dimensional numerical method had to be developed for coupling the finite volume and discrete element methods in the analysis of flexible and elastic structures. With this purpose in mind, two similar numerical methods were developed in order to simulate two specific types of structure. Each one of them was designed for different functions, and involved different dynamic behaviors. As there was a wealth of information already collected in real, physical experiments that measured the behavior of loose elements in a fish net tunnel, and that served as a way of contrasting the numerical models with the behavior of fluids in a natural setting, the theoretical framework for those experiences was used as a reference for the potential divergences between simulations and real conditions.

5.1 Fish Net

The preliminary results show that the coupled method for solving the interaction between the fishnet, free bodies and water performs qualitatively well, obtaining a similar shape of the Fish Net Tunnel than the one adopted in the towing tank. The model is able to represent the coupled behavior and interaction between the fishnet, the fishing load and the fluid. The mesh angle shows a contraction at the middle of the net, and in the bulb takes higher values as expected.

The combination of direct computation of drag and induced mass forces

for the smaller fishnet elements, and use of immersed boundary method for the larger freely moving objects seems to perform adequately.

Further research is required to quantitatively assess the accuracy of the method, more rigorous towing tank, in order to tune the spring rates and the tuning coefficient of the load radius, should be performed to reproduce the expected mesh angles along the net. Further, the computational efficiency of the method can be improved, incorporating a parallel implementation of the DEM, coupled with the already parallel CFD method.

5.2 Vorticity Wind Turbine

For the modeling of the VWT, bending moment transmission was incorporated to the already developed DEM applied to the fish net, whereas the elements of the fishnet are loose ropes, so there is no bending moment transmission in between the elements. Another important variation applied to the method was the approach used for integrating the equations of motion. In the case of the fishnet, a fourth order Runge-Kutta was implemented for solving the ordinary differential equations system, while for the VWT a centered finite difference, as the proposed by Ivanov (2001), was used for the integration. It would be interesting, in order to improve the computational efficiency of the simulation, to incorporate a higher order method, such as the one used for the fishnet system, or even to consider the incorporation of an adaptive time step, a potential future development that was beyond the scope of this research.

The three-dimensional coupled method for elastic and flexible structures seems to represent qualitatively well the dynamics of the VWT. The amplitude of the oscillations obtained in the simulations is consistent with the results of the structural calculations from Section 3.1, as it was expected to obtain oscillations with an approximated amplitude of 1.4 times the diameter at the top end of the mast, compared to the amplitude of twice the diameter from the simulation.

Another indication of the consistency of the model is that the frequency of the oscillation (f) is practically the same to the vortex shedding frequency (f_{vs}), managing to capture the lock-in effect. And the vortex shedding frequency is similar to the frequency calculated from the Strouhal number (St), tabulated for cylinders as a function of the Reynolds number.

Although the displacement of the device is well captured for the transversal

direction, it has to be taken into consideration that the study does not involve all the parameters of a real situation, as in this simulation the force in the along wind direction would not be transmitted to the rod, because the measurement of the displacement in this direction is not considered relevant for the study. Drag forces acting over the mast are quantitatively important, and they would produce larger displacements in the stream-wise direction, this effect has not been studied in this research.

However, this could be improved, for instance with a limiting hoop around the rod. This is a physical and practical solution, and the representation in the numerical model would be feasible by limiting the motion of the rod within a hoop of radius R_{lim}, if the position of the last bar of the rod (r) is greater or equal to R_{lim}, then only the component $(F_{e\theta})$, perpendicular to (r), of the immersed boundary force (F_{imb}) is taken in consideration. Which is exactly the kind of limitation that would be imposed to the movement in real settings by an actual hoop.

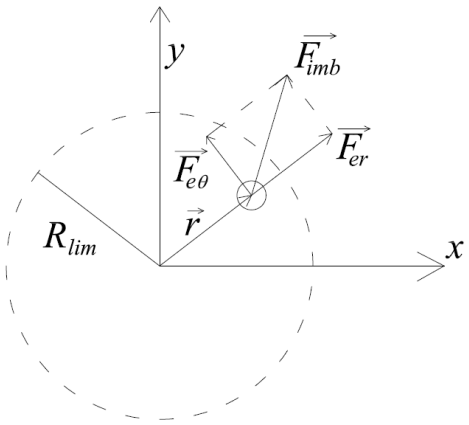

Figure 5.1: Scheme of the limiting hoop

The limiting hoop was partially tested in the model, but the performance was not as predictable as expected, and further research is needed, so that modification to the device was not included in the simulations for the results presented here. With respect to this, is worth clarifying that the modeling of the generator that has been implemented is rather simple and performs well for linear displacements only. If the aim was to harvest energy from displacements in every direction, then other kind of power take off system should be considered, for instance a joystick-type generator that could generate with any angular displacement.

Anyway, the simulation for the implemented generator performs quantitatively well, with values that are comparable in terms of peak and integrated efficiencies to the ones presented by Bernitsas et al. (2008b,a) in experimental physical tests for the VIVACE generator. Even taking into consideration that, at least in the simulation stage, the vorticity turbines is less efficient than current blade turbines, the practicality of the method in terms of cost, simplicity of the installation, maintenance and affordability of updates and enhancements, makes it a convenient and scalable solution that could complement rather well other conventional means.

It should also be said that the conical shape of the mast was designed as a means to achieve a perfect synchronization of the vortex shedding all along the mast. Considering that the wind velocity increases with height in the atmospheric boundary layer, the diameter of the oscillating structure should also increase with height to favor the synchronization. In this research, only uniform flows have been tested, but it would be very enriching to simulate the efficiency of this devices under the dynamics of an atmospheric boundary layer. Also further research would allow to determine the most efficient shape for the mast to optimize the synchronization and therefore maximize the output power. Nevertheless, the lock in effect was well captured in the simulations, and synchronization was roughly achieved for the uniform flow. But there is plenty of room for increasing accuracy in upcoming studies looking at the same technology, incorporating new variables and more precise models, and obtaining more predictive simulations.

It is worth mentioning the potential of the method to predict output power for this type of systems, because the ability to test different designs or types of applications would be easily implemented just by introducing the corresponding changes in the code. For instance, those incorporations could allow testing a more sophisticated power take off system or even considering the adaptation of the device to produce energy underwater, harvesting the motion of waves and currents.

Finally, with further research the computational method could be modified to make a more complete representation of the dynamics in the rotor of a conventional wind turbine. The method would allow to analyze in greater detail the behavior of the blades by dividing them in many parts (that would be analog to the representation of the rod in this work), and accounting both normal and shear force, as well as bending and torsional moments in between

each element composing the blade. With this implementation, a simulation of a wind turbine rotor would provide meaningful results, more consistent with reality, in terms of the mechanics of the blade as a deformable solid, and its interaction with the fluid, with the correspondent extract of power from the fluid. Such a model would allow to evaluate the elastic behavior of the blade, including its effect on to energy production. Still, further research in the methods of simulation would be required to achieve this goal.

Bibliography

Advisory Committee on Technical Recommendations for Construction (2010). Guide for the assessment of wind actions and effects on structures. *National Research Council of Rome, Italy*.

Balash, C., Colbourne, B., Bose, N., and Raman-Nair, W. (2009). Aquaculture net drag force and added mass. *Aquacultural Engineering*, 41(1):14–21.

Balash, C., Sterling, D., Binns, J., Thomas, G., and Bose, N. (2016). Drag characterisation of prawn-trawl bodies. *Ocean Engineering*, 113:18–23.

Barrero-Gil, A., Pindado, S., and Avila, S. (2012). Extracting energy from vortex-induced vibrations: A parametric study. *Applied Mathematical Modelling*, 36(1):3153–3160.

Bearman, P. (2011). Circular cylinder wakes and vortex-induced vibrations. *Journal of Fluids and Structures*, 27(1):648–658.

Bernitsas, M., Ben-Simon, Y., Raghavan, K., and Garcia, E. (2008a). The vivace converter: model tests at high damping and reynolds number 10^5. *Journal of Offshore Mechanics and Arctic Engineering*, 130(1):1–15.

Bernitsas, M., Raghavan, K., Ben-Simon, Y., and Garcia, E. (2008b). Vivace (vortex induced vibration aquatic clean energy): a new concept in generation of clean and renewable energy from fluid flow. *Journal of Offshore Mechanics and Arctic Engineering*, 130(1):1–15.

Bi, C.-W., Zhao, Y.-P., Dong, G.-H., Xu, T.-J., and Gui, F.-K. (2014). Numerical simulation of the interaction between flow and flexible nets. *Journal of Fluids and Structures*, 45:180 – 201.

Cajas, J., Houzeaux, G., Yáñez, D., and Mier-Torrecilla, M. (2016). Shape project vortex bladeless: Parallel multi-code coupling for fluid structure

interaction in wind energy generation. *Partnership for Advanced Computing in Europe*.

Cundall, P. and Strack, O. (1979). A discrete numerical model for granular assemblies. *Geotechnique*, 29(1):47–65.

Donoso, G., Ladera, C., and Martin, P. (2010). Magnetically coupled magnet-spring oscillators. *European Journal of Physics*, 31(1):433–452.

Fadlun, E., Verzicco, R., Orlandi, P., and Mohd-Yusof (2000). Combined immersed-boundary finite-difference methods for three-dimensional complex flow simulations. *Journal of Computational Physics*, 161:35–60.

Ferziger, J. H. and Peric, M. (2002). *Computational Methods for Fluid Dynamics*. Springer-Verlag Berlin Heidelberg New York, Germany.

Govardhan, R. and Williamson, C. (2006). Defining the 'modified griffin plot' in vortex-induced vibration: revealing the effect of reynolds number using controlled damping. *Journal of Fluid Mechanics*, 561(1):147–180.

Griffin, O. M., Skop, R. A., and Ramberg, S. E. (1975). The resonant, vortex-exited vibrations of structures and cables systems. *Offshore Technology Conference*, 7(1).

Hockney, R. W. and Eastwood, J. W. (1988). *Computing Simulation Using Particles*. IOP.

Ivanov, R. I. (2001). *Analysis of Structures by the Three Dimensional Discrete Element Method*. Doctor of philosophy, University of Kobe, Japan.

Klamo, J. T., Leonard, A., and Roshko, A. (2005). On the maximum amplitude for a freely vibrating cylinder in crossflow. *Journal of Fluid Mechanics*, 363(1):97–114.

Lange, C. F., Schäfer, M., and Durst, F. (2002). Local block refinement with a multigrid flow solver. *International Journal for Numerical Methods in Fluids*, 38(1):21 – 41.

Lee, C.-W., Lee, J.-H., Cha, B.-J., Kim, H.-Y., and Lee, J.-H. (2005). Physical modeling for underwater flexible systems dynamic simulation. *Ocean Engineering*, 32(3-4):331–347.

Lehnhäuser, T. and Schäfer, M. (2002). Improved linear interpolation practice for finite-volume schemes on complex grids. *International Journal for Numerical Methods in Fluids*, 38(7):625 – 645.

Lehnhäuser, T. and Schäfer, M. (2003). Eficient discretization of pressure-correction equations on non-orthogonal grids. *International Journal for Numerical Methods in Fluids*, 42(2):211 – 231.

Liao, C.-C., Chang, Y.-W., Lin, C.-A., and McDonough, J. (2010). Simulating flows with moving rigid boundary using immersed-boundary method. *International Journal for Numerical Methods in Fluids*, 39(1):152 – 167.

Lilek, Z., Muzaferija, S., Peric, M., and Seidl, V. (1997). An implicit finite-volume method using nonmatching blocks of structured grid. *Numerical Heat Transfer, Part B: Fundamentals*, 32(4):385 – 401.

Mendina, M., Draper, M., Soares, A. P. K., Narancio, G., and Usera, G. (2014). A general purpose parallel block structured open source incompressible flow solver. *Cluster Computing*, 17(2):231 – 241.

Mittal, R. and Iaccarino, G. (2005a). Immersed boundary methods. *Annual Review of Fluid Mechanics*, 37(1):239 – 261.

Mittal, R. and Iaccarino, G. (2005b). Immersed boundary methods. *Annu. Rev. Fluid Mech.*, 37:239–261.

Mohd-Yusof, J. (1998). Development of immersed boundary methods for complex geometries. *Center of Turbulence Research*, Annual Research Briefs:325–336.

Parkinson, G. V. (1972). Mathematical models of flow-induced vibrations of bluff bodies. In *Flow-Induced Structural Vibrations - IUTAM-IAHR Symposium Karlsruhe*, pages 81–127, Berlin.

Peskin, C. S. (1972). Flow patterns around heart valves: A numerical method. *Journal of Computational Physics*, 10:252–271.

Peskin, C. S. (1982). The fluid dynamics of heart valves: Experimental, theoretical and computational methods. *Annual Review of Fluid Mechanics*, 14(2):235.

Peskin, C. S. (2002). The immersed boundary method. *Acta Numerica*, pages 479–517.

Priour, D. (1999). Calculation of net shapes by the finite element method with triangular elements. *Communications in Numerical Methods in Engineering*, 15(10):755–763.

Priour, D. (2009). Numerical optimisation of trawls design to improve their energy eficiency. *Fisheries Research*, 98(1-3):40 – 50.

Shimizu, T., Takagi, T., Korte, H., Hiraishi, T., and Yamamoto, K. (2007). Application of nala, a fishing net configuration and loading analysis system, to bottom gill nets. *Fisheries Science*, 73(3):489–499.

Smagorinsky, J. (1963). General circulation experiments with the primitive equations. *Monthly Weather Review*, 91(3):99 – 164.

Soti, A. K., Thompson, M. C., Sheridan, J., and Bhardwaj, R. (2017). Harnessing electrical power from a vortex-induced vibration of a circular cylinder. *Journal of Fluids and Structures*, 70(1):360–373.

Takagi, T., Shimizu, T., and Korte, H. (2007). Evaluating the impact of gillnet ghost fishing using a computational analysis of the geometry of fishing gear. *ICES Journal of Marine Science: Journal du Conseil*, 64(8).

Takagi, T., Shimizu, T., Suzuki, K., Hiraishi, T., Matsushita, Y., and T.Watanabe (2003). Performance of "nala"; a
fishing net shape simulator. *Fisheries Engineering*, 40(2):125–134.

Usera, G., Vernet, A., and Ferré, J. A. (2006). Use of time resolved piv for validating les/dns of the turbulent flow within a pcb enclosure model. *Flow, Turbulence and Combustion*, 77(1):77 – 95.

Usera, G., Vernet, A., and Ferré, J. A. (2008). A parallel block-structured finite volume method for flows in complex geometry with sliding interfaces. *Flow, Turbulence and Combustion*, 81(3):471.

Williamson, C. H. K. and Govardhan, R. (2008). A brief review of recent results in vortex-induced vibrations. *Journal of Wind Engineering and Industrial Aerodynamics*, 96(1):713–135.

Zaleski, S. (2001). Science and fluid dynamics should have more open sources. *online*.

APPENDICES

Appendix 1

Structural Analysys

For making the along-wind and across wind calculations, it is needed to firstly characterize the local wind that will act over the studying structure, this is where the structure is located or where it is expected to build it.

1.1 Wind Velocity and Pressure

In order to obtain the design values of wind and calculating the Peak Wind Velocity Pressure the next steps are made according to the data given in the *Guide for the assessment of wind actions and effects on structures*, Advisory Committee on Technical Recommendations for Construction (2010). This data corresponds to measurements made in Italy, but as in the case of the vorticity wind turbines, the expectations are to place them not only in a specific place, this data is used for the characterization.

1.1.1 Basic reference wind velocity

It is define as the maximum value of the 10-minute mean wind velocity at a height of $10\,m$ above flat open country with roughness length $z_0 = 0.05\,m$, for a design return period $T_R = 50$ years. Due to the lack of specific data, that takes into account site roughness, terrain topography and wind direction, the basic reference wind velocity v_b is given by Eq. 1.1, where the basic reference wind velocity at sea level is $v_{b,0} = 27m/s$, and the altitude coefficient is $c_a = 1$, thus:

$$v_b = v_{b,0} \cdot c_a = 27m/s \tag{1.1}$$

1.1.2 Design return period and design reference velocity

Is the maximum value of the 10-minute mean wind velocity in same conditions as the previous section, for a design return period $T_R = 50$ years. Once again, in the lack of accurate data, equation 1.2 is used, where the return coefficient $c_r = 1$.

$$v_r = v_b \cdot c_r = 27\,m/s \tag{1.2}$$

1.1.3 Exposure category

It is assume that these devices are built in areas with roughness class D, occasional isolated obstacles, such as open countryside, farmlands or pastures. According to this the exposure category is II, with the following coefficients values:

$$k_r = 0.19 \quad z_0 = 0.05\,m \quad z_{min} = 4\,m$$

1.1.4 Topography coefficient

This coefficient considers the contraction of the wind at the top of hills or the funneling in valleys. In this case as the site is open country the topography coefficient is $c_t = 1$.

1.1.5 Mean Velocity

This value depends on the height above ground, and the exposure category. For heights not exceeding $z = 200\,m$ the mean wind velocity profile, with $T_R = 50$ years, is given by equation 1.3.

$$v_m(z) = v_r \cdot c_m(z) \tag{1.3}$$

Where c_m is the mean wind velocity profile coefficient provided by equation 1.4

$$c_m(z) = k_r \cdot Ln\left(\frac{z_{min}}{z_0}\right) \cdot c_t(z_{min}) = 0.833 \qquad \text{for} \quad z \leqslant z_{min} \tag{1.4a}$$

$$c_m(z) = k_r \cdot Ln\left(\frac{z}{z_0}\right) \cdot c_t(z) = 0.19 \cdot Ln\left(\frac{z}{0.05}\right) \qquad \text{for} \quad z > z_{min} \tag{1.4b}$$

And then, the mean wind velocity profile is,

$$v_m(z) = 22.49\, m/s \qquad \text{for} \quad z \leqslant z_{min} \tag{1.5a}$$

$$v_m(z) = 5.13 \cdot Ln\left(\frac{z}{0.05}\right) \qquad \text{for} \quad z > z_{min} \tag{1.5b}$$

The mean wind velocity profile associated with the design retun periods $T_R =$ 1 year and $T_R = 500$ years, can be determined by multipling this profile, respectively, by the return coefficients $c_r = 0,75$ and $c_r = 1,207$.

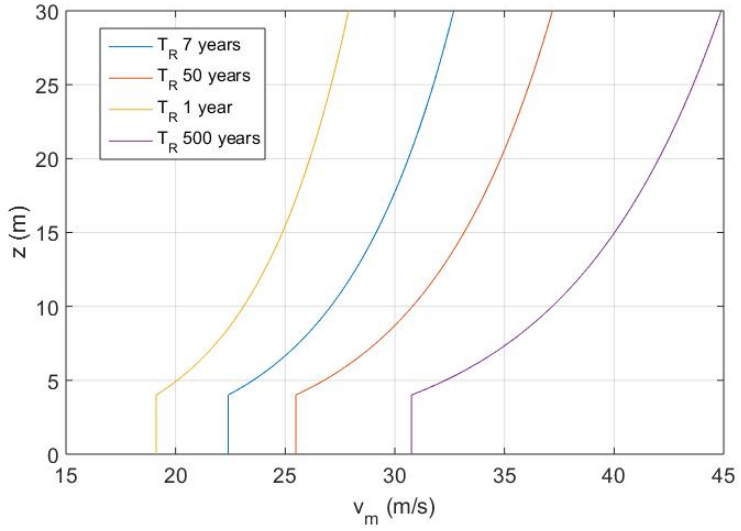

Figure 1.1: Graph of the mean wind velocity for returns periods of 1, 7, 50 and 500 years

1.1.6 Atmospheric turbulence

The turbulence intensity is the standard deviation of the longitudinal turbulent component divided by the mean wind velocity.

$$I_v(z) = \left[Ln\left(\frac{z_{min}}{z_0}\right) \cdot c_t(z_{min})\right]^{-1} = 0.228 \qquad \text{for} \quad z \leqslant z_{min} \tag{1.6a}$$

$$I_v(z) = \left[Ln\left(\frac{z}{0.05}\right)\right]^{-1} \qquad \text{for} \quad z > z_{min} \tag{1.6b}$$

The turbulence length scale represents the average size of the eddies formed

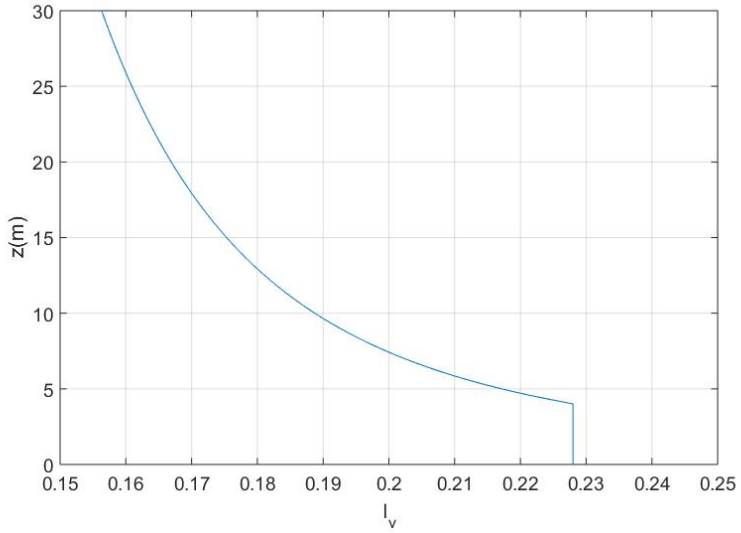

Figure 1.2: Graph of the turbulence intensity

in the atmospheric turbulence.

$$L_v(z) = \overline{L} \cdot \left(\frac{z_{min}}{\overline{z}}\right)^k = 39.23 \qquad \text{for} \quad z \leqslant z_{min} \tag{1.7a}$$

$$L_v(z) = \overline{L} \cdot \left(\frac{z}{\overline{z}}\right)^k = 300 \cdot \left(\frac{z}{200}\right)^{0.52} \qquad \text{for} \quad z > z_{min} \tag{1.7b}$$

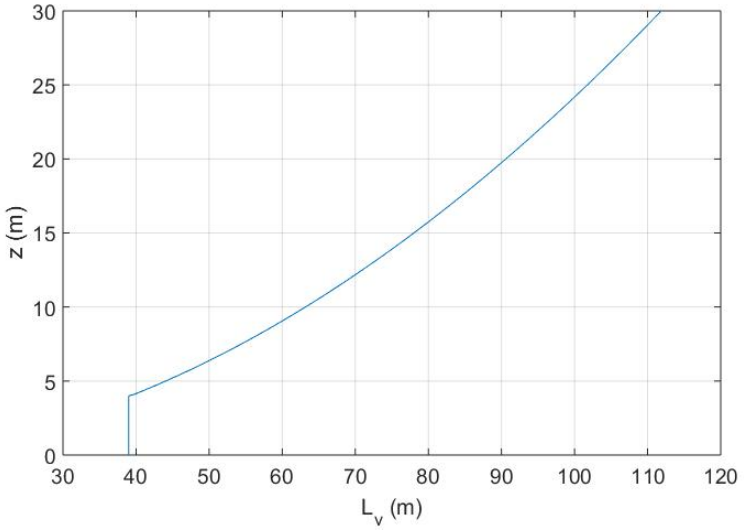

Figure 1.3: Graph of the integral length of turbulence

1.1.7 Peak velocity pressure

The peak wind velocity pressure q_P is the expected value of the maximum wind velocity pressure over a time $T = 10min$.

$$q_p(z) = 1/2\,\rho\, v_r^2\, c_e(z) \tag{1.8}$$

Where ρ is the air density ($\rho = 1.25\,kg/m^3$) and $c_e(z)$ is the exposure factor given by the equation:

$$c_e(z) = k_r^2 \cdot Ln\left(\frac{z_{min}}{z_0}\right) \cdot c_t(z_{min}) \cdot \left[Ln\left(\frac{z_{min}}{z_0}\right) \cdot c_t(z_{min}) + 7\right] \quad \text{for} \quad z \leqslant z_{min} \tag{1.9a}$$

$$c_e(z) = k_r^2 \cdot Ln\left(\frac{z}{z_0}\right) \cdot c_t(z) \cdot \left[Ln\left(\frac{z}{z_0}\right) \cdot c_t(z) + 7\right] \quad \text{for} \quad z > z_{min} \tag{1.9b}$$

Calculating with the values in previous sections the coefficient c_e takes the following form:

$$c_e(z) = 1.80 \quad \text{for} \quad z \leqslant z_{min} \tag{1.10a}$$

$$c_e(z) = 0.036 \cdot Ln\left(\frac{z}{0.05}\right) \cdot \left[Ln\left(\frac{z}{0.05}\right) + 7\right] \quad \text{for} \quad z > z_{min} \tag{1.10b}$$

Thus, the peak wind velocity pressure for a return period $T_R = 50$ years is:

$$q_p(z) = 820\,N/m^2 \quad \text{for} \quad z \leqslant z_{min} \tag{1.11a}$$

$$q_p(z) = 16.4 \cdot Ln\left(\frac{z}{0.05}\right) \cdot \left[Ln\left(\frac{z}{0.05}\right) + 7\right] \quad \text{for} \quad z > z_{min} \tag{1.11b}$$

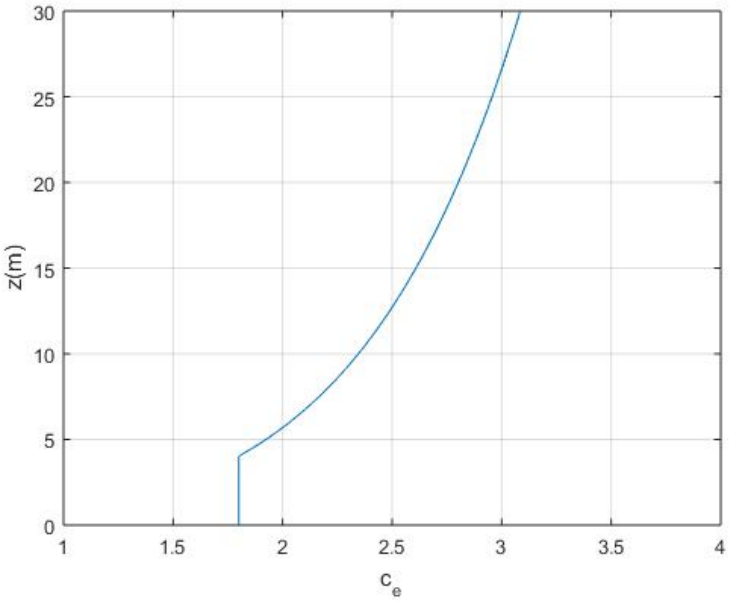

Figure 1.4: Graph of the Exposure coefficient

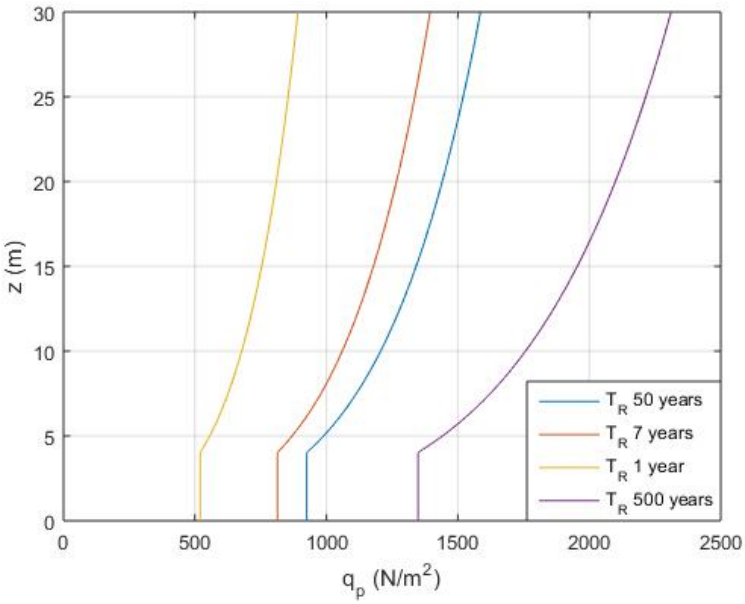

Figure 1.5: Graph of the peak wind velocity pressure for return periods of 1, 7, 50 and 500 years

1.2 Actions in the along-wind direction

The document first determines the aerodynamic actions in the along-wind direction. For this the peak aerodynamic action per unit length is expressed in Eq. (1.12), where $q_P(z)$ = peak wind velocity pressure; l = the reference length; c_{f_X} = the force coefficient per unit length, calculated in Eq. (1.13).

$$f_X(z) = \quad q_P(z) \cdot D(z) \cdot c_{f_X} \tag{1.12}$$

$$c_{f_X} = \quad c_{f_{Xo}}(Re) \cdot \Psi_\lambda \tag{1.13}$$

Here $c_{f_{Xo}}$ is the coefficient per unit length for structures of infinite length, and Ψ_λ takes account of edge reduction effects. These coefficients are calculated as expressed in Eq. (1.14) to Eq. (1.16). Note that the same calculations can be done to the transversal component force in $y-$direction and the torsional moment in $z-$direction, which results theoretically zero in structures with polar symmetry.

$$c_{f_X\,o} = 1.255 + \frac{0.197 \cdot \log\left(10 \cdot k/D\right)}{1 + 0.4 \cdot \log\left(Re/10^6\right)} \tag{1.14}$$

$$\Psi_\lambda = 0.45 + 0.25 \cdot \log \lambda \tag{1.15}$$

$$\lambda = \frac{L}{D_{ref}} \tag{1.16}$$

Here k is the roughness of the surface, $k = 0.005mm$ for a carbon-glass fiber polished surface; and λ is the slenderness factor. As the coefficient per unit length, c_{fXo}, depends on the Reynolds number, which depends of the wind velocity and the diameter of the structure, both variable with z, the calculations are made at 14 different heights, results are resumed in Table 1.1.

For the calculation of the equivalent along wind static force, Eq. (1.17), the critical damping ratio is previously calculated as the sum of the structural and aerodynamic damping ratios, $\xi = \xi_s + \xi_a$, where ξ_s is tabulated for the different materials and ξ_a is calculated with properties of the structure and flow. With this the dynamic factor is calculated, c_{dD}.

$$F_D = f_X \cdot L \cdot c_{dD} \tag{1.17}$$

$$c_{dD} = \frac{G_D}{1 + 7 \cdot I_v(z_e)} \tag{1.18}$$

Table 1.1: Resumed calculations of the Peak aerodynamic action per unit length of the VWT

z [m]	d [m]	vm (m/s)	Re	cfXo	cfx	fx [N/m]
1	0.1	22.49	145,097	0.277	0.227	11.1
2	0.500	22.49	725,484	0.420	0.344	111.3
3	0.542	22.49	785,941	0.425	0.348	140.6
4	0.583	22.49	846,398	0.430	0.352	168.0
5	0.625	22.49	906,855	0.434	0.355	194.7
6	0.667	24.56	1,056,337	0.450	0.369	227.4
7	0.708	25.35	1,158,496	0.458	0.375	256.9
8	0.750	26.04	1,259,789	0.464	0.380	286.5
9	0.792	26.64	1,360,638	0.470	0.385	316.2
10	0.833	27.18	1,461,310	0.475	0.389	346.2
11	0.875	27.67	1,561,977	0.479	0.392	376.5
12	0.917	28.12	1,662,755	0.483	0.396	407.0
13	0.958	28.53	1,763,723	0.487	0.399	437.9
14	1.000	28.91	1,864,934	0.490	0.402	469.0

$$G_D = 1 + 2 \cdot g_D \cdot I_v(z_e) \cdot \sqrt{B^2 + R_R^2} \tag{1.19}$$

Here G_D = along wind gust factor; $I_v(z_e)$ = turbulence intensity at the reference height; d_D = along wind peak factor; B = background factor; R_R = resonant response factor. Following Eq. (1.20) to Eq. (1.26) F_D can be calculated.

$$B^2 = \frac{1}{1 + 0.9 \cdot \left(\frac{D_{ref}+L}{L_v(z)}\right)^{0.63}} \tag{1.20}$$

$$R_R^2 = \frac{\pi}{4\xi_s} S_D \cdot R_L \cdot R_D \tag{1.21}$$

$$S_D = \frac{6.868 \cdot \ f_N \cdot L_v(z_e)/v_m(z_e)}{\left[1 + 10.32 \cdot \ f_N \cdot L_v(z_e)/v_m(z_e)\right]^{5/3}} \tag{1.22}$$

$$R_L = \frac{1}{\eta_L} - \frac{1}{2\eta_L^2}\left(1 - \exp^{-2\eta_L}\right) \quad \text{with} \quad \eta_L = 4\,\frac{f_N \cdot L}{v_m(z_e)} \tag{1.23}$$

$$R_D = \frac{1}{\eta_D} - \frac{1}{2\eta_D^2}\left(1 - \exp^{-2\eta_D}\right) \quad \text{with} \quad \eta_D = 4\,\frac{f_N \cdot D_{ref}}{v_m(z_e)} \tag{1.24}$$

$$g_D = \sqrt{2 \cdot \ln(v_D \cdot T)} + \frac{0.5772}{\sqrt{2 \cdot \ln(v_D \cdot T)}} \tag{1.25}$$

$$v_D = f_N \cdot \sqrt{\frac{R_R^2}{B^2 + R_R^2}} \tag{1.26}$$

Where $L_v(z_e)$ = turbulence length scale; T = mean wind velocity averaging time, $T = 600s$. Table 1.2 summarize the calculations towards the value of c_{dD}.

Table 1.2: Resumed calculations for determining the Dynamic Factor for the VWT

Equation	**Parameter**
	$L_{tot} = 14\,m$
Figure 3.1	$D_{ref} = 0.77\,m$
	$z_e = 8.4\,m$
Eq. (1.5)	$v_m(z_e) = 26.06m/s$
Eq. (1.6)	$I_v(z_e) = 0.196$
Eq. (1.7)	$L_v(z_e) = 154.71$
Figure 3.2a	$f_N = 2.09Hz$
Section 3.1	$\xi = 0.008$
Eq. (1.20)	$B^2 = 0.83$
Eq. (1.22)	$S_D = 0.0252$
Eq. (1.23)	$\eta_L = 4.49$
Eq. (1.24)	$\eta_D = 0.343$
Eq. (1.23)	$R_L = 0.198$
Eq. (1.24)	$R_D = 0.806$
Eq. (1.21)	$R_R^2 = 0.3948$
Eq. (1.26)	$v_D = 1.187$
Eq. (1.25)	$g_D = 3.784$
Eq. (1.19)	$G_D = 2.642$
Eq. (1.18)	$c_{dD} = 1.114$

The equivalent along wind static force is the product of the peak aerodynamic actions and the dynamic coefficient. So integrating along the vertical axis of the structure (using Table 1.1) for a value of $c_{dD} = 1.114$, $F_D = 3,377\,N$.